

Constraining carbon loss from rivers following terrestrial enhanced rock weathering

Shuang Zhang¹, Christopher T Reinhard², Shaoda Liu³, Yoshiki Kanzaki², and Noah J Planavsky^{4,5}

¹Department of Oceanography, Texas A&M University

²School of Earth and Atmospheric Sciences, Georgia Institute of Technology

³School of Environment, Beijing Normal University

⁴Department of Earth and Planetary Sciences, Yale University

⁵Yale Center for Natural Carbon Capture, Yale University

March 15, 2024

1 **Main Manuscript for**

2
3 **Constraining carbon loss from rivers following terrestrial enhanced rock weathering**

4
5 Shuang Zhang^{a,1}, Christopher T. Reinhard^b, Shaoda Liu^c, Yoshiki Kanzaki^b, Noah J. Planavsky^{d,e}

6
7 ^aDepartment of Oceanography, Texas A&M University, College Station, TX, USA

8 ^bSchool of Earth and Atmospheric Sciences, Georgia Institute of Technology, Atlanta, GA, USA

9 ^cSchool of Environment, Beijing Normal University, Beijing, China

10 ^dDepartment of Earth and Planetary Sciences, Yale University, New Haven, CT, USA

11 ^eYale Center for Natural Carbon Capture, Yale University, New Haven, CT, USA

12
13 ***Corresponding author:** Shuang Zhang

14 **Email:** shuang-zhang@tamu.edu

15
16 **Author Contributions:** S.Z., N.J.P., and C.T.R. designed research; S.Z. performed research; S.L.
17 provided the river $p\text{CO}_2$ data; S.Z. analyzed data and contributed new modeling tools; S.Z.,
18 N.J.P., and C.T.R. wrote the paper, with contributions from S.L. and Y.K.

19
20 **Competing Interest Statement:** The authors declare no competing interest.

21
22 **Classification:** Physical Sciences (Major); Earth, Atmospheric, and Planetary Sciences (Minor)

23
24 **Keywords:** carbon dioxide removal; enhanced rock weathering; river degassing; carbon cycle;
25 climate mitigation

26
27 **This PDF file includes:**

28 Main Text

29 Figures 1 to 3

45 **Abstract**

46

47 Enhanced rock weathering (EW) has garnered increasing interest as a promising technique for
48 durable carbon dioxide removal, with a range of potential co-benefits including increased soil pH
49 and nutrient release. However, the impacts of EW on river chemistry and the potential loss of
50 initially captured CO₂ during river transport remain poorly constrained. The current lack of tools
51 for robustly predicting the effect of riverine degassing on the EW life cycle undermines the use of
52 this practice as a carbon mitigation strategy. Here, we present results from a first-of-its-kind
53 dynamic river network model designed to quantify the impact of EW on river carbonate chemistry
54 in North American watersheds. We map key water quality parameters across the river network of
55 North America using machine learning, and use a dynamic river network model to simulate
56 changes in river carbonate chemistry and carbon degassing during EW. Our model predicts low
57 carbon loss (<5%) from river networks and limited changes to carbonate mineral saturation states
58 for many of the river pathways explored here. However, there are some instances in which carbon
59 degassing is significantly higher (>15%) and it is possible to induce large changes in carbonate
60 saturation states, indicating that riverine carbon storage and the impacts of EW on river chemistry
61 must be evaluated in a deployment-specific context. Although there remains uncertainty in the
62 impact of EW on stream/river chemistry, our approach represents a step forward in the
63 development of tools for quantifying the impacts of carbon cycling in downstream catchments on
64 the overall EW lifecycle.

65

66 **Significance Statement**

67

68 Enhanced rock weathering (EW) has emerged as a promising long-term carbon dioxide removal
69 (CDR) method with potential soil and crop co-benefits. However, its impact on river chemistry
70 and the potential loss of captured CO₂ during river transport is unclear. We have developed a
71 dynamic river network model to evaluate EW's effects on North American watersheds. Following
72 EW application to a preliminary example set of locations, many rivers show low carbon loss and
73 limited carbonate saturation state change. However, regional variation exists, emphasizing the
74 need for deployment-specific evaluation and further development of process-based models of
75 stream/river carbon cycling. This study provides a step forward in the development of tools for
76 quantifying the impact of EW on river systems, supporting the potential for large-scale EW, and
77 informing CDR strategy decisions and carbon markets.

78

79

80

Main Text

81

82 **Introduction**

83

84 There is growing recognition of the need for durable (long-duration) carbon dioxide removal (CDR)
85 to meet climate targets in the coming century (1–3). Terrestrial enhanced rock weathering (EW)
86 — the intentional application of crushed alkaline (carbonate or silicate) rock to soil to drive
87 fixation of atmospheric CO₂ as dissolved bicarbonate (HCO₃⁻) — has been suggested to offer a
88 scalable, relatively low cost form of CDR with durability on thousand-year timescales (4–8). The
89 potential magnitude of carbon removal through EW, though still poorly defined, may rival or
90 surpass terrestrial ecosystem sequestration (e.g., via afforestation or soil organic carbon storage)

91 and is potentially >5 gigatons of CO₂ (GtCO₂; 10⁹ tons) per year (5, 9–11). Because EW uses
92 existing technology and infrastructure, it is ready to deploy and has potential for achieving
93 relatively rapid scale alongside other efforts to help meet net-zero greenhouse gas emission goals.
94 EW's potential for widespread adoption is further enhanced by a number of possible co-benefits,
95 including enhancing crop growth via an increase in soil pH and improved availability and uptake
96 of macro and micronutrients, reducing CO₂ emissions associated with traditional fertilizer
97 production, and possible mitigation of soil emissions of nitrous oxide (e.g., 12–14).

98
99 Despite the potential of EW as an effective CDR strategy, there are still significant uncertainties
100 that prevent generation of robust carbon removal from this practice, including the lack of a
101 framework to track the downstream fate of carbon captured at the site of weathering. Foremost,
102 there is no existing framework for tracking the dynamics of solute transport and storage through
103 river networks following EW deployment. Although recent work has explored the first-order
104 response of carbonate mineral saturation in river systems and its implications for carbon leakage
105 (11, 15, 16), it is likely that the riverine carbon and solute transport following EW deployment will
106 be impacted by CO₂ gas exchange between the river and the atmosphere upon mixing of multiple
107 reach-scale river segments with varying dissolved inorganic carbon (DIC) and alkalinity (ALK)
108 content (17). Integrated over the catchment scale, this process has the potential to significantly
109 impact the overall efficacy of EW in sequestering atmospheric CO₂. In addition, existing work has
110 focused on individual and disconnected rivers or watersheds, and there is no existing framework
111 for tracking EW solute fluxes across catchment scales that incorporates river network topology
112 and reach-scale interconnections in a time-dependent manner.

113
114 Here, we develop a dynamic river network (DRN) model that is designed to track the transport and
115 transformation of EW products through river systems from the reach to the continent scale. The
116 DRN model builds upon existing river network delineation (e.g., 18, 19) and uses comprehensive
117 data sources, machine learning methods, and reaction-transport principles to achieve predictions
118 of key river hydrochemistry parameters following EW deployment. We focus here on tracking the
119 impacts of EW on the North American rivers, but once fully developed and validated the
120 framework can in principle be applied to any region of interest given rapid advances in the global
121 reach of digital elevation models (DEMs) and river network data.

122 123 **Building the DRN model framework**

124
125 There are four key steps in constructing the DRN model (Fig. S1). First, we compile key water
126 quality parameters from existing river stations across the contiguous United States (CONUS).
127 Second, we build the river network topology by connecting river segments that either flow through
128 the CONUS or receive water from rivers flowing through the CONUS. We define this set of river
129 segments as our North American river network. Third, we use machine learning to predict the key
130 water quality parameters for the whole North American river network based on the discrete water
131 quality dataset and their corresponding watershed properties as a training set. Lastly, we construct
132 the DRN model based on the predicted key water quality parameters, river
133 hydrology/geomorphology, and reconstructed *p*CO₂ values from prior analysis. Once configured,
134 this DRN model can then be used to dynamically track river responses to introduction of solutes
135 from EW.

137 To establish the baseline chemistry (before implementing EW) of North American rivers, we
 138 assimilate hydrogeochemistry data for the CONUS from the United States Geological Survey
 139 (USGS) (20), including comprehensive data for ALK, Ca, pH, salinity, and water temperature (Fig.
 140 S2). Based on these parameters, the monthly baseline carbonate saturation state values (Ω) for the
 141 CONUS rivers can be calculated (Fig. S3). To interpolate the spatially disconnected
 142 hydrogeochemistry data into a seamless reach-scale river network across North America, we first
 143 extract North American river network and topology data from the Global Reach-scale A priori
 144 Discharge Estimates for SWOT (GRADES) river network (18). This extensive network offers
 145 detailed global river reach topology and morphology (such as channel slope), along with daily
 146 discharge estimates at the reach scale over a 35-year period. Based on GRADES, we determine
 147 the monthly river surface area and volume (Fig. S4) of each river segment (*Materials and Methods*).
 148 We then employ a random forest (RF) machine learning algorithm, which can predict key water
 149 quality parameters (ALK, Ca, salinity, and water temperature) throughout the North American
 150 river network from compiled North American watershed parameters (i.e., climate-hydrology
 151 parameters, lithology, land cover, geomorphology, and soil properties) (Fig. S5-S8). We
 152 subsequently merge the water quality parameters predicted by the RF model, together with river
 153 discharge, surface area, and volume, with the river $p\text{CO}_2$ values reconstructed in prior work by ref.
 154 (19) to form a single consolidated dataset. This dataset serves two purposes: first, to compute the
 155 background monthly carbonate system (for example, DIC and carbonate saturation state) and CO_2
 156 degassing flux for each river segment across North America; and second, to be utilized
 157 subsequently in the DRN model.

158
 159 After consolidating the river network data, we proceed to construct a system of ordinary
 160 differential equations (ODEs) (Eq. 1–4) tracking the carbon budget in each discrete river segment.
 161 This ODE system (the DRN model) treats each river segment as a single reservoir and explicitly
 162 tracks tracer fluxes (DIC, ALK, Ca, and salinity) through and between reservoirs following EW
 163 implementation:

$$165 \quad \frac{d\text{DIC}}{dt} = F_{up_DIC} - F_{down_DIC} - F_{degass_DIC} + F_{other_DIC} + F_{EW_DIC} \quad (1)$$

$$167 \quad \frac{d\text{ALK}}{dt} = F_{up_ALK} - F_{down_ALK} + F_{other_ALK} + F_{EW_ALK} \quad (2)$$

$$169 \quad \frac{d\text{Ca}}{dt} = F_{up_Ca} - F_{down_Ca} + F_{other_Ca} + F_{EW_Ca} \quad (3)$$

$$171 \quad \frac{d\text{Salinity}}{dt} = F_{up_Salinity} - F_{down_Salinity} + F_{other_Salinity} + F_{EW_Salinity} \quad (4)$$

172
 173 where F_{up} terms trace the flux from the joining upstream reach, F_{down} terms trace the flux flowing
 174 out of the current reach, F_{other} terms represent “residual” partitioning fluxes within each reach
 175 (implicitly including carbonate precipitation and net carbon metabolism), which can be solved
 176 inversely using a mass balance approach (*Materials and Methods*), and F_{EW} traces the solute flux
 177 derived from EW. The DIC mass balance contains an additional term — F_{degass} — which

178 represents the carbon exchange flux between a given river reach and the atmosphere and can be
179 calculated using the following equation.

180

$$181 \quad fCO_2 = k \cdot ([CO_2]_r - [CO_2]_a) \quad (5)$$

182

183 where $[CO_2]_r$ represents the CO_2 concentration in river, $[CO_2]_a$ represents the CO_2 concentration
184 in river that is in equilibrium with the atmosphere, and k represents the gas transfer velocity at the
185 water–air interface. The k value for each river segment is quantified based on its flow regime (low-
186 vs. high-energy streams) using channel slope, flow velocity, and water temperature as parameters
187 (21–23) (*Materials and Methods*).

188

189 The ODE system (Eq. 1–4) allows us to track dynamic changes to river chemistry in any
190 downstream reach in response to the input of EW products into any river segment. Coupling the
191 dynamic evolution of DIC, ALK, Ca, and salinity with other river properties (e.g., water
192 temperature, surface area) allows us to solve the complete system of carbonate species, the
193 carbonate saturation state, and carbon degassing flux for each river reach through time.
194 Subsequently, the cumulative carbon leakage with time for each river flow path can be calculated.
195 (*Materials and Methods*).

196

197 **Tracking river responses to EW using the DRN model**

198 Prior to deploying our DRN model to simulate the river responses to EW, we first assess the
199 model’s ability to capture background monthly fluctuations in river chemistry. As a case study, we
200 use the longest Mississippi flow path to compare model predictions with actual monthly river
201 signals for randomly chosen river segments. Encompassing a broad spectrum of spatial scales,
202 diverse lithological characteristics, and varied climatic conditions, the Mississippi river and its
203 watershed function as a multifaceted natural laboratory. Coupled with its extreme river data density
204 (24), this flow path provides a useful baseline for validating the performance of our DRN model.
205 We run the model from day 0 for each river segment along the Mississippi flow path for two years
206 without any EW input, utilizing a time step of 0.1 day, then compare the modeled DIC and ALK
207 time series with the background monthly DIC and ALK values from empirical data.

208

209 We next introduce EW solutes into a randomly selected river segment in North America and run
210 our DRN model to track the downstream river chemistry change and carbon degassing (e.g.,
211 carbonate saturation state and carbon degassing flux). The model outcome also enables us to
212 monitor integrated carbon leakage during the transport of EW solutes along the entire flow path.
213 In our simulation, basalt serves as the EW feedstock. Owing to its fast reaction rate, relatively high
214 Mg and Ca content, and widespread availability, basalt is often chosen as the primary rock type
215 for EW applications (5, 25). After basalt is spread to the watershed of river segment, we assume it
216 dissolves congruently and all dissolved solutes enter the selected river segment. The dissolution
217 rate is set as 1 ton of basalt per hectare per year in our baseline scenario, a reasonable assumption
218 that is comparable to previous modeling and field studies (5, 9, 26). We then multiply this assumed
219 dissolution rate by the watershed area of the selected river segment to determine the total annual
220 input of basalt solutes into the river segment. From this, the daily input of basalt solute into the
221 river segment is derived and fed into our DRN model. Notably, applying this dissolution rate to
222 the global land surface would result in a global basalt dissolution flux of 15 Gt/yr. Although this

223 global enhanced basalt dissolution rate falls within the range of recent estimates of the global river
224 capacity to transport dissolved from basalt weathering without inducing carbonate precipitation
225 (11), we do not advocate for the likelihood of any particular scenario here. Instead, this value is
226 only meant to illustrate a scenario of relatively large-scale EW deployment. We also emphasize
227 here that the basalt dissolution rate adopted in this study is not determined by mechanistic reaction
228 kinetics. However, the DRN model is designed to be flexibly coupled with solute fluxes derived
229 from field measurements or reaction-transport models of soil biogeochemistry.

230
231 After setting up the EW input to the selected river segment, we run our DRN model over 2 years
232 to determine the changes in river chemistry and carbon leakage for the whole flow path through
233 time. To examine the regional differences in carbon leakage due to incoming EW solutes, we
234 repeated the model simulation with 100 different random river segments. These 100 different river
235 segments are sampled with equal probability from all North American river segments and broadly
236 cover the climatic and hydrogeochemical heterogeneity of the North American continent. For each
237 river segment, we apply basalt to its corresponding watershed and set the basalt dissolution rate at
238 1 ton per hectare per year in the baseline scenario. This rate is then multiplied by the watershed
239 area of the river segment (Fig. S9A) to calculate the total annual input of basalt solutes into the
240 river segment (Fig. S9B). Our DRN model is run over 2 years for each segment to assess the river
241 chemistry change and carbon leakage through time. In total, we conduct 100 DRN model runs over
242 the North American river network.

243

244 **Sensitivity tests of the DRN model**

245 We conduct 10 sensitivity tests of the DRN model to assess the impact of river discharge and gas
246 transfer velocity (k) values on the simulated carbon leakage rate across the river network. First, we
247 randomly sample the monthly discharge values for each river segment 10 times, adhering to a
248 normal distribution based on the mean and standard deviation provided by GRADES. Concurrently,
249 k values are recalculated for each set of resampled discharge values (see *Materials and Method* for
250 the relationship between k and discharge). We then reconstruct the DRN model and perturb it with
251 EW at each of the selected 100 sites, employing each set of resampled discharge values and the
252 recalculated k values. The carbon leakage from these 10 iterations is quantified and compared to
253 the DRN model output for the baseline scenario. We also explore two additional basalt dissolution
254 scenarios — targeting 0.5 ton of basalt dissolved per hectare per year and 1.5 ton of basalt dissolved
255 per hectare per year, respectively — to test model sensitivity to variations in the magnitude of EW.
256 We define the 0.5 ton as the low scenario and the 1.5 ton as the high scenario.

257

258

259 **Results and Discussion**

260

261 **River chemistry and carbon degassing in North America**

262 Our compiled river chemistry data provide broad spatial coverage across the CONUS,
263 comprehensively representing its geographical diversity (Fig. S3). The prior distribution of
264 carbonate saturation state values (Ω) in U.S. rivers is strongly right-skewed (Fig. S3). In January,
265 84% of the Ω values are below 5, and 96% are below 10; in July, these numbers are 76% and 90%,
266 respectively. The slightly higher Ω values in the summer reflect the aggregate impacts of seasonal
267 shifts in river chemistry and hydroclimatic parameters. In particular, increased temperature

268 (leading to lower CO₂ solubility), accelerated background chemical weathering in watersheds (and
269 thus greater alkalinity flux into rivers), and human activities (intensified agricultural practices and
270 wastewater discharge) all impact seasonal shifts in Ω , and these will vary based on the specific
271 geography and ecology of each river segment. Across all months, 81% of the Ω values are below
272 5, and 93% are below 10.

273
274 The RF model performs reasonably well at predicting key water quality properties at the reach
275 scale from assimilated USGS gauging stations (Fig. S5-S8). For all target variables (i.e., ALK, Ca,
276 salinity, and water temperature), the trained model produces $R^2 > 0.75$ when applied to the test
277 data, suggesting that our framework is capable of explaining more than 75% of the inherent
278 variability in the target variables of unobserved river stations. By utilizing the consolidated dataset
279 that includes river ALK, Ca, salinity, and water temperature predicted by the RF model, along with
280 the river channel slope, discharge, surface area, volume, and $p\text{CO}_2$ values, we can solve the whole
281 carbonate system (for example, DIC and CO_3^{2-}) for each river segment and reconstruct the monthly
282 carbon degassing flux and carbonate saturation states across the North American river network
283 (Fig. 1). The calculated carbon degassing flux reveals a considerable degree of spatial
284 heterogeneity and strong temporal fluctuations (Fig. 1A,C). For example, the degassing flux varies
285 spatially among segments from -0.02 to 19 gC m⁻² d⁻¹ and between 5×10^{-7} to 31 gC m⁻² d⁻¹ for
286 January and July, respectively. The degassing flux observed in July generally exceeds that in
287 January, consistent with ref. (19), which can be linked to higher river $p\text{CO}_2$ levels and elevated gas
288 transfer velocity during summertime, as well as seasonal variations in watershed hydrology.
289 Similarly, the reconstructed Ω values across North America exhibit substantial spatial and temporal
290 variation. Values in July typically surpass those in January (Fig. 1B,D). Overall, the distribution
291 of Ω values is right skewed, with the majority falling below 10 — comprising 84% in January and
292 80% in July. These low background Ω values suggest *a priori* that the North America river network
293 possesses a significant capacity to assimilate EW solutes without inducing significant net
294 carbonate precipitation, as carbonate precipitation in river waters tends to be negligible when Ω is
295 below ~ 10 , and in many cases insubstantial carbonate precipitation is observed in systems with Ω
296 values well above 10 (16, 27–29).

297
298

299 **Model performance in reconstructing background river chemistry and carbon degassing**

300 We observe close correspondence between DRN model predictions and background monthly
301 dissolved ALK and DIC (which in turn constrain the carbonate system) for the 1st, 200th, 400th,
302 600th, and 771st river segments along the longest Mississippi flow path (Fig. S10). Specifically, the
303 monthly averaged relative error for DIC ranges from 0.012% to 0.14% for our benchmark
304 segments. For ALK, the range is also 0.012% to 0.14% for the same segments. This agreement
305 indicates the F_{other} terms in Eq. 1-4 are solved accurately and our DRN model could reconstruct
306 the background river chemistry before any ERW input. Comparison of predicted monthly carbon
307 degassing with observation-based estimates (e.g., calculated gas exchange fluxes based on discrete
308 solute measurements) for river segments in central Connecticut and New Hampshire (30, 31)
309 yields an $R^2 = 0.7$ (Fig. S11). Although our predicted values and the observation-based estimates
310 are generally in agreement, measurement-based estimates still bear large uncertainty (as evidenced
311 by the big error bar in Fig. S11), making the comparison with model predictions challenging.
312 Comprehensive empirical constraints on stream/river CO₂ gas exchange for validation of this and
313 other predictive models of inland water CO₂ cycling is an obvious future research topic.

314

315 **River leakage following EW and the controlling factors**

316 With EW applied at each of the 100 random sites (Fig. 2A) individually over 2 years, the DRN
317 model tracks the downstream responses for each flow path through time. As expected, the longer
318 flow paths tend to exhibit a higher predicted total carbon degassing flux (Fig. S12). However,
319 cumulative carbon leakage, defined as the ratio of additional carbon degassed from the river to the
320 atmosphere compared with carbon degassed in the background state relative to the total DIC added
321 to the headwater following the EW application (*Materials and Methods*), is generally below 5%
322 for the baseline scenario. The cumulative leakage experiences a steep increase at the beginning of
323 the model simulation and then remains relatively unchanged throughout the simulation period (Fig.
324 2B). After applying EW for durations of 6, 12, 18, and 24 months, the percentages of flow paths
325 with cumulative carbon leakage rates < 5% are 91%, 99%, 93%, and 94%, respectively (Fig. 2C).
326 Two flow paths out of the 100 simulated here exhibit significantly higher leakage rates.
327 Specifically, path 1 experiences carbon leakage approaching 20% and path 2 exceeds 5% carbon
328 leakage for the majority of the model simulation period. The maximum cumulative leakage rate
329 for the baseline scenario stands at 20.3%. The additional 10 sensitivity tests associated with this
330 scenario reveal carbon leakage patterns closely aligned with those observed in the initial baseline
331 output (Fig. S13). Across the 100 flow paths, the maximum cumulative carbon degassing fluctuates
332 between approximately 20.2% and 23.6% for these tests, with most flow paths showing low carbon
333 leakage throughout the simulation period. After 24 months, 93% of river flow paths exhibit carbon
334 leakage below 5% in the 10 sensitivity tests. Similarly, the low and high scenarios demonstrate
335 carbon leakage patterns that are consistent with the baseline scenario (Fig. S14). We also observe
336 that carbon leakage is smaller in the low scenario compared to the baseline scenario, while carbon
337 leakage is higher in the high scenario compared to the baseline scenario.

338

339 The median carbonate saturation state (Ω) for each of the flow paths in the baseline scenario
340 remains low and is largely unaltered after EW application when compared with the background
341 state at each duration (Fig. 2D). However, much like the seasonal fluctuations observed in the
342 background data, the carbonate saturation state is higher overall during summer months (after 6 or
343 18 months) than winter months (after 12 or 24 months) (Fig. 2D), which is potentially attributable
344 to increased temperature, accelerated background chemical weathering in watersheds, and human
345 activities. After the continuous application of EW for either 6 or 18 months, approximately 66%
346 of the river flow paths displayed median Ω values less than 10, and approximately 92% displayed
347 Ω values less than 15. In contrast, following 12 or 24 months of continuous EW application, around
348 86% of all river segments exhibited median Ω values below 10, and approximately 97% displayed
349 Ω values less than 15. Nonetheless, some flow paths showed extremely high Ω values ($\Omega > 100$),
350 particularly in the first sediments downstream of EW deployment (Fig. S15), indicating a clear
351 need for a better understanding of calcium carbonate formation and recycling in bedload sediments
352 under transient extremes in carbonate saturation state.

353

354 Our study indicates a strong positive association between the median cumulative carbon leakage
355 rates and median carbonate saturation states across flow paths for sustained durations
356 encompassing 6, 12, 18, and 24 months (Fig. S16A). This relationship predominantly originates
357 from the strong positive correlation between alkalinity and carbonate saturation states in the river
358 (Fig. S16B), and the impact of alkalinity on carbon degassing. We argue that the EW DIC:ALK
359 ratio and their absolute amounts, coupled with the unique hydrological attributes of the river

360 segments, control the dynamics of carbon leakage rates during EW implementation. Implementing
361 an EW input with a DIC:ALK ratio of 1, as adopted by this study (*Materials and Methods*), will
362 lead to an increase in the $p\text{CO}_2$ value in the river, as dictated by the thermodynamic relations
363 involving DIC, ALK, and the equilibrium fluid $p\text{CO}_2$ (Fig. S17). Consequently, the river will shift
364 towards more carbon degassing, resulting in a leakage of carbon from the river system (Fig. 2B).
365 Furthermore, larger input of DIC and ALK will result in commensurately greater elevation in
366 riverine $p\text{CO}_2$ (Fig. S17), fostering increased degassing and, consequently, enhanced carbon
367 leakage. The elevated leakage rates exhibited by the two flow paths discussed above (Fig. 2B) can
368 be explained by the temporal patterns of alkalinity in those river segments (Fig. S18A), which are
369 in turn governed by the ratio of the alkalinity flux to the flow path volume over time (Fig. S18B).
370 Similarly, the varying carbon leakage rates across the three basalt dissolution scenarios (Fig. S14)
371 can also be attributed to differences in the alkalinity fluxes into the river segments, with higher
372 leakage rates associated with higher alkalinity flux.

373
374 Being the recipient of basalt dissolution products, the first river segment is poised to respond more
375 swiftly to EW applications, making it an ideal focal point for examining the interactions between
376 EW applications and river responses. The fluctuation in a river segment's alkalinity can be
377 modulated by various factors including the alkalinity input flux and the river flow dynamics. Not
378 surprisingly, after alkalinity injection, we observe a positive correlation ($r = 0.58$) between the
379 alkalinity input flux and the shift in alkalinity, relative to the concurrent background state, in the
380 first segment (Fig. S19A). At the same time, we observe a strong negative correlation ($r = -0.76$)
381 between the segment volume and the shift in alkalinity (Fig. S19B). Theoretically, segments with
382 either a smaller volume or a higher influx of basalt dissolution products from EW will exhibit a
383 more pronounced response due to a more dramatic increase in the ALK (as well as DIC)
384 concentration. Here, a surge in alkalinity in the first segment is directly associated with elevated
385 leakage rates after day 1 ($r = 0.81$; Fig. S20). This rapid response of the first segment to the
386 incoming EW solutes also accounts for the sharp increase in carbon leakage rate observed at the
387 onset of our model simulation (Fig. 2B). In summary, our findings suggest that carbon leakage is
388 predominantly controlled by both EW input fluxes and the hydrological conditions of individual
389 river segments, with seasonal variations in flow dynamics playing a significant role in determining
390 fluctuation in carbon leakage rate across systems.

391

392 **Spatial heterogeneity of river leakage and river chemistry following EW**

393 Following the HydroSHEDS watershed delineation scheme (32), we subdivide the river flow paths
394 explored here into seven watershed regions across North America—Middle, North, Northeast,
395 Northwest, South, Southeast, and Southwest (Fig. 3). This allows us to quantify the variations in
396 cumulative carbon leakage rate and carbonate saturation state across these regions. The median
397 cumulative carbon leakage rate of the flow paths after 24 months of EW application in our
398 randomized deployment scheme increases in the following order: Southeast (0.6%), Northeast
399 (1.4%), North (1.7%), Northwest (2.5%), Middle (2.8%), South (4.7%), and Southwest (4.9%)
400 (Fig. 3A). The median carbonate saturation state of the flow paths increases in a similar order:
401 Southeast (0.02), Northeast (0.9), Northwest (1.9), North (3.6), Middle (4.0), Southwest (9.1), and
402 South (10.3) (Fig. 3B). Our study finds a positive correlation between median cumulative carbon
403 leakage rates and median carbonate saturation states in various regions (Fig. S21). This finding
404 aligns with the observed positive correlation between carbon leakage rates and carbonate
405 saturation states across individual flow paths (Fig. S16A), supporting the strategic selection of

406 river watersheds with low initial carbonate saturation for real-world EW application. Such rivers
407 not only accommodate EW products more effectively but also exhibit lower carbon leakage,
408 maximizing EW's net impact on atmospheric CO₂ sequestration. The distribution of cumulative
409 carbon leakage rates is irregular both within each region and among different regions (Fig. 3C),
410 implying significant heterogeneity in river hydrochemistry and watershed properties. Notably, the
411 southwest region, which displays the highest median carbon leakage rate, also encompasses the
412 two flow paths that exhibit the highest carbon leakage rates among the 100 flow paths studied here
413 (Fig. 2B). This phenomenon is likely to be attributed to the pronounced evapotranspiration and dry
414 conditions in the southwest, which lead to diminished river flow and storage, thereby amplifying
415 the impact of EW on solute chemistry and facilitating higher leakage rates. Spatial heterogeneity
416 is also evident in the carbonate saturation state of all river segments, both within each region and
417 across different regions (Fig. 3D). This strong heterogeneity in carbonate saturation state and river
418 leakage rate indicates a need to use deployment-specific information for any EW project
419 attempting to create carbon offsets, as specific deployment regions and flow paths can potentially
420 be characterized by much larger CO₂ degassing than the aggregate statistics would imply.

421

422 **Implications for evaluating river/stream CO₂ leakage in EW deployments**

423 In aggregate, our results suggest limited carbon leakage during riverine carbon transport and
424 relatively low carbonate saturation state in the river network during EW application. Nonetheless,
425 spatial heterogeneity is evident and non-trivial carbon leakage in rivers is ubiquitous, and in some
426 cases can be large, such that any compensatory claims on CO₂ emissions made based on the
427 generation of EW-based carbon credits need to explicitly take this carbon loss into account or
428 measure it empirically. Although the current DRN framework does not explicitly account for
429 changes in carbonate precipitation resulting from the addition of EW products to river systems,
430 our simulations show generally very small changes in the carbonate saturation state of most rivers
431 despite very high assumed total EW solute fluxes. In addition, it is possible that carbonate formed
432 at the reach scale will subsequently dissolve in bedload sediments due to extensive CO₂ production
433 from aerobic respiration (33, 34). Nonetheless, more realistic deployment scenarios than that
434 explored here — in particular situations in which one or multiple suppliers are operating at scale
435 in a relatively small region — could potentially lead to dramatic changes in carbonate saturation
436 states that lead to more carbonate precipitation than the background state. For example, our results
437 clearly show that initial river segments downstream of EW solute release see much larger changes
438 to carbonate saturation state (Fig. S15) than other segments (Fig. 2D) downstream. This provides
439 additional rationale for assessing the impact of individual EW projects on surface waters in a
440 deployment-specific context and the need for full data transparency in EW projects. Further, this
441 work also strongly suggests that new frameworks to prevent the overuse of a common good—
442 rivers—will need to be established.

443

444 By elucidating the riverine responses to EW, we can also more accurately define the boundary
445 conditions for river fluxes to the ocean under various EW scenarios (35). Interestingly, as inferred
446 from the thermodynamic relationships involving DIC, ALK, and equilibrium *p*CO₂ (Fig. S17), a
447 river flow path experiencing increased carbon degassing during the transport of EW products will
448 exhibit a lower DIC:ALK ratio in its final flux to the ocean. This, in turn, will mitigate the rise of
449 *p*CO₂ levels in the seawater upon receiving the river flux, resulting in reduced carbon degassing
450 from the seawater to the atmosphere (or possibly resulting in ingassing). In other words, our results
451 imply that carbon leakage from river systems and subsequent loss from the surface ocean (7) are

452 not additive, and that carbon loss during riverine transport will decrease net carbon loss to
453 degassing in the surface ocean. The exception to this dynamic would be large-scale cation removal
454 during transport to the coastal ocean through secondary carbonate or clay formation, which
455 remains an important topic for future research. In any case, our model sets the stage for future
456 modeling efforts aimed at understanding the ocean's response to EW products transported by rivers
457 in a regional, deployment-specific context.

458
459 The presented DRN model framework is meant to be a step forward in the development of tools
460 that can provide a more realistic and comprehensive assessment of the impact of EW. However,
461 there are still uncertainties in our ability to accurately predict river/stream degassing of CO₂ across
462 a range of relevant scenarios—and a need to further validate this model framework with large-
463 scale EW trials. Our analysis should not be taken as an indication that a relatively minor discount
464 to field CDR rates can be uniformly applied to compensate for the effects of EW on rivers
465 regardless of deployment strategy or location. Future studies should focus on refining the DRN
466 model by incorporating the dynamics of carbonate precipitation in response to the addition of EW
467 products, as stressed by ref. (15). Additionally, the model should be enhanced by integrating more
468 comprehensive carbon cycling processes, such as metabolic activity (36–38). Lastly, coupling the
469 DRN framework with mechanistic models of upstream processes, such as feedstock dissolution in
470 soils and cation storage and transport in the lower vadose zone, will be required to provide more
471 realistic predictions of the impacts of EW on river chemistry and catchment-scale degassing.

472 473 **Conclusion**

474
475 We introduce a dynamic river network model designed to explore the impacts of EW on river
476 systems across scales. In aggregate, results from a quasi-randomized EW deployment scenario
477 yielded relatively minor shifts to carbonate mineral saturation states in most downstream river
478 segments, but the potential for high degree of supersaturation locally. Overall carbon leakage, from
479 carbonic acid system re-equilibration, was found to be generally below 5% throughout the two-
480 year simulation period across North American watersheds. However, impacts will be region- and
481 deployment-specific, and it will be important to validate these results with empirical observations
482 and additional simulations with more realistic deployment architectures. Nonetheless, this work
483 represents a step forward in understanding and predicting the carbon degassing of river networks
484 and the water chemistry impacts of EW. Moving forward, further development of open tools such
485 as the DRN network presented here has the potential to inform policy decisions and be utilized in
486 carbon marketplaces, highlighting the value of continuing to investigate, refine, and critically
487 interrogate all aspects of the EW process.

488 489 **Materials and Methods**

490 491 **River data compilation**

492
493 We collect a suite of river chemical species and properties (ALK, Ca, salinity, pH, water
494 temperature and discharge) through the CONUS from USGS (20). We select eleven different
495 parameter codes for alkalinity (00418, 00421, 29801, 29802, 29803, 39036, 39086, 39087, 99431,
496 00410 and 90410), two parameter codes for calcium (00915 and 91051), three parameter codes for
497 salinity (i.e., total dissolved solids) (70300, 70301 and 00515), three parameter codes for pH

498 (00400, 00403, and 00408), and one parameter code for temperature (00010) according to the
 499 USGS parameter coding system. To calculate flux-weighted species concentration, we further
 500 collect river discharge rates (parameter code 00060). For each of these parameters, we remove the
 501 samples that are not labeled as “Surface Water” from our river sample dataset. We further calculate
 502 the average value of each of the parameters for the samples that have the same “ActivityIdentifier”.
 503 Outlier data, defined as values higher than the 99th percentile of each parameter, are removed. Sites
 504 with multiple measurements in a day are averaged on a daily basis for each parameter, after which
 505 all parameters are matched together based on the unique site number and sampling date. To
 506 maintain a high-quality monthly signal, we remove the sites that lack at least one data point for
 507 each month. After data filtering, the monthly value of each parameter for each river station is
 508 calculated by aggregating the samples by month, weighted by the discharge rate. We further
 509 remove the river sites that do not have drainage area recorded in the USGS database. This yields
 510 our final dataset for river chemistry, which contains 1995 river sites, and each site contains 12
 511 monthly values for each property. The distribution of each river property can be found in Fig. S2.
 512 Complete monthly carbonate system (such as $[CO_3^{2-}]$) then could be solved from the monthly ALK,
 513 pH, salinity, and water temperature at each site using the *seacarb* package (39), considering the
 514 impact of both temperature and salinity. Subsequently, calcite saturation state (Ω) in the 1995 sites
 515 (Fig. S3) could be calculated based on solute chemistry, temperature, and salinity according to the
 516 following equation (11):

$$\Omega = \frac{[Ca^{2+}][CO_3^{2-}]}{K_{sp}} \quad (S1)$$

519 where K_{sp} represents the apparent solubility product for calcite corrected for site-specific
 520 temperature and salinity (40) and brackets denote concentration. Eq. S1 is also used in the DRN
 521 model to calculate the evolution of Ω values in each river segment. We only present calcite Ω
 522 values given the argonite, dolomite, and other carbonate minerals are unlikely to precipitate.

524 **Building the river network in North America**

526
 527 We use the Global Reach-scale A priori Discharge Estimates for SWOT (GRADES) river network
 528 (18) to build the river topology in North America. GRADES provides a topology of global river
 529 reaches (close to 3 million individual ones), coupled with estimates of daily discharge at each reach
 530 scale, spanning across a substantial 35-year period. It has the length (L), watershed boundary, and
 531 connectivity to other segments for each river segment. We overlay the watersheds of GRADES on
 532 the CONUS and extract the ones that intersect with the CONUS. We then extract the final water
 533 outlets for all those watersheds and further extract all the river segments whose final outlets match
 534 those watershed outlets. Specifically, wherever we apply EW on the CONUS land surface, the
 535 downstream flow path is contained in this data set.

536 Based on the river connectivity, we delineate the whole downstream flow path starting from each
 537 river segment for the North America, which paves the way for us to feed into the EW solutes to
 538 any segment and to track the downstream response. The monthly width of the river segment is
 539 derived from ref. (19), estimated by integrating both the downstream hydraulic geometry (DHG)
 540 and at-a-station hydraulic geometry (AHG) relationships for width. With the segment length and
 541 monthly width, we calculate the monthly segment surface area (Fig. S4A,C). Following ref. (19),

542 the flow velocity for each segment is estimated from monthly discharge and a gauge-derived
 543 discharge-velocity (Q-V) relationship (i.e., $\ln V = 0.12 \ln Q - 1.06$) (41), which predicts reliable
 544 velocity over a broad range of river discharge (0.01 to 20,000 m³ s⁻¹). With monthly river discharge
 545 and flow velocity, we calculate the monthly cross section area (A) of each segment (i.e., $A = Q/V$)
 546 and further calculate the monthly volume of each segment (i.e., $\text{Volume} = A * L$) (Fig. xx)

547
 548 Gas transfer velocity (k) is estimated from channel slope and flow velocity, which together
 549 correspond to the decaying dissipation energy (ϵ_D) along river networks and have been shown to
 550 be able to predict reasonable k over large spatial scales in various regions (23). We use a slope
 551 cutoff of 0.01 (19) to differentiate low- vs. high-energy alpine streams (21), and calculate the k
 552 value for these two types of streams separately.

553
 554 For streams not affected by high bubble-mediated gas exchanges in steep terrains, k was estimated
 555 directly from channel slope and flow velocity (22):

$$556 \quad k_{600} = 2841SV + 2.02 \quad (S2)$$

557
 558 where k_{600} is the gas transfer velocity at a common Schmidt number (Sc) of 600 (for CO₂, the
 559 Schmidt number at around 20 °C), S is channel slope (m/m) and V is flow velocity (m/s).
 560 Specifically, channel slope is directly from the GRADES river networks. Flow velocity is derived
 561 by coupling monthly discharge from the GRADES dataset to a gauge-derived Q-V relationship as
 562 shown above.
 563

564
 565 For streams affected by high bubble-mediated gas exchanges in steep terrains, k was estimated
 566 using a reported power law relationship between k_{600} and the dissipation energy (ϵ_D , m² s⁻³) (21):

$$567 \quad \ln(k_{600}) = 1.18 \ln(\epsilon_D) + 6.43 \quad (S3)$$

$$568 \quad \epsilon_D = gSV$$

569
 570 where g is gravitational acceleration (m s⁻²).

571
 572 Finally, the following relationship is used to convert estimated k_{600} to gas transfer velocity (k) at
 573 specific temperatures for each month.
 574

$$575 \quad k_{in\ situ} = k_{600} \left(\frac{Sc_{CO_2}}{600} \right)^{-2/3} \quad (S4)$$

576
 577 where 600 is the Schmidt number of CO₂ in freshwater at 20 °C. Sc_{CO_2} is the Schmidt number for
 578 CO₂ at specific temperatures in freshwater and can be calculated as:

$$579 \quad Sc_{CO_2} = 1742 - 91.24T_w + 2.208T_w^2 - 0.0219T_w^3 \quad (S5)$$

580
 581 where water temperature (T_w in °C) is estimated (along other key water quality parameters) from
 582 machine learning in this study.
 583
 584
 585
 586

587 **Watershed property compilation**

588

589 We compile a suite of watershed properties used to predict the water properties (Ca, ALK, salinity
590 and water temperature) over North America. First, we delineate the total upstream watershed for
591 each river segment based on the river topology and individual watershed for each segment. Second,
592 for each delineated upstream watershed, we calculate the average value of watershed properties,
593 including monthly temperature and precipitation (42), monthly runoff (43), monthly soil moisture
594 (44), surface lithology (45), land cover (46), land erosion rate (47, 48), soil pH and organic carbon
595 content (49), net primary productivity (50), and nitrification rate (51). Third, we match the
596 collected river stations (from USGS) to the appropriate river segment. To achieve this, we search
597 within a 20 km radius centered on each river station to find the nearest river segment. We ensured
598 that this segment's total upstream watershed area is similar to the drainage area provided by the
599 USGS, allowing for a difference of less than 50%. After snapping, we extract the watershed
600 properties for each river station from the already compiled watershed properties over the whole
601 North America river network. Finally, we merge the river chemistry at each river station with its
602 corresponding watershed properties into a dataset that will be used to train a machine learning
603 framework. The watershed properties over the whole river network in the North America will be
604 fed into the trained machine learning framework to map the river properties over North America.
605

606 **Mapping river properties over the North American river network using machine learning**

607

608 We employ the Random Forest (RF) algorithm, a tree-based ensemble supervised machine learning
609 technique that offers several advantages over other machine learning techniques, including low
610 bias and moderate variance (52). RF is based on decision tree, which is a non-parametric
611 supervised learning algorithm used for classification or regression. Decision tree captures non-
612 linear relationships in the data and is robust to input outliers (53). However, decision trees can also
613 be prone to overfitting (i.e., high variance), relatively low in predictive accuracy and does not yield
614 optimal solutions. RF can be thought of an ensemble of many trees (called the bagging technique),
615 and it reduces the high variance experienced by a single decision tree. Different than simple
616 bagging, RF further decorrelates the trees by using a random set of predictor variables to divide
617 the training data during each splitting. All these modifications contribute to the high predictive
618 accuracy (low bias and moderate variance) of RF. The RF algorithm has been widely used in
619 geoscience research (e.g., 52) and is particularly suitable for making predictions using high
620 dimensional data with complex non-linear relationships, such as our dataset.
621

622 The construction of the RF model is conducted in R (55) using the “ranger” package (56). We build
623 a regression domain, in which the monthly river Ca concentration, ALK, salinity, and temperature
624 are the target variables and the potential factors (watershed properties) that influence those river
625 parameters are the predictor variables. We split the whole data into a training dataset (75% of the
626 data) and a test dataset (the remaining 25% of the data). The training set, as the name suggests, is
627 used to train the model — allowing it to learn the relationship between the predictor variables and
628 the target variable. The testing set, on the other hand, is employed to evaluate the performance of
629 the model on unseen data, providing an estimate of how accurately the model would predict with
630 new data. During the training process, we select 500 for num. trees (i.e., the number of sub-models)
631 and 3 for min.node.size (i.e., the minimal size of the tree branch in each sub-model) as our model
632 hyperparameters. After model training and testing, we retrain the model on the whole dataset. This

633 final model, trained on all available data, is considered to have optimized learning from the given
 634 dataset, and thus should offer the best possible performance when deployed to handle real-world
 635 data. We then feed the compiled watershed properties over the whole river network in North
 636 America into the final machine learning model to obtain the Ca, ALK, salinity and water
 637 temperature over the North America river network. These water properties are joined with
 638 previously modeled river $p\text{CO}_2$ values (19) to further quantify the background monthly carbonate
 639 system chemistry and carbon degassing flux for each river-reservoir segment (Fig. 1).

640

641 DRN model setup

642

643 The DRN model is designed to be able to quantify the dynamics in the carbonate system (carbon
 644 mixing, saturation state shifts, and carbon degassing) in each river segment downstream following
 645 the application of EW in any watershed. The core of the DRN model is the ODE system (Eq. 1-4).
 646 First, we need to make sure our DRN model could reconstruct the background river dynamics
 647 before running any EW simulation. Accordingly, the initial equations (Eq. 1–4) will be modified
 648 to:

649

$$650 \quad \frac{dDIC}{dt} = F_{up_DIC} - F_{down_DIC} - F_{degass_DIC} + F_{other_DIC} \quad (S6)$$

651

$$652 \quad \frac{dALK}{dt} = F_{up_ALK} - F_{down_ALK} + F_{other_ALK} \quad (S7)$$

653

$$654 \quad \frac{dCa}{dt} = F_{up_Ca} - F_{down_Ca} + F_{other_Ca} \quad (S8)$$

655

$$656 \quad \frac{dSalinity}{dt} = F_{up_Salinity} - F_{down_Salinity} + F_{other_Salinity} \quad (S9)$$

657

658 As F_{up} , F_{degass} , and F_{down} can all be calculated directly from our synthesized river parameters,
 659 the key step to complete the whole ODE system is to inversely calculate the term F_{other} , which
 660 can be readily finished following the mass balance equation. Specifically, we interpolate the
 661 monthly signal of all river parameters (e.g., DIC, ALK, salinity, Ca, water temperature, river
 662 surface area, river volume, river discharge) to daily signal using the monotone Hermite spline
 663 method (57), which yields a much more smooth spline than the linear interpolation method. Then,
 664 we calculate the value of the derivative (e.g., $\frac{dDIC}{dt}$) as well as the F_{up} , F_{degass} , and F_{down} at each
 665 day and then solve F_{other} at each day for each tracer based on mass balance. Specifically, F_{other}
 666 at each day can be easily obtained by calculating the difference between $\frac{dDIC}{dt}$ and $F_{up} + F_{degass} +$
 667 F_{down} . Finally, we build the function for F_{other} change with time, which will be further used in
 668 the forward ODE equations (both the background Eq. S6–S9, or EW Eq. 1–4). To test whether our
 669 DRN model could reconstruct the background river dynamics, we pick the longest flow path in
 670 North America (the Mississippi river) and ran our ODE system (Eq. S6-S9) for this flow path from
 671 day 0 for 2 years. To run the ODE, we utilized the “vode” ode solver in the “deSolve” package
 672 (58). The “vode” solver, also known as the Variable-coefficient Ordinary Differential Equation
 673 solver, is particularly effective in handling “stiff” ODE problems. To further enhance the model

674 accuracy, we decreased the relative error tolerance from the default 1e-6 to 1e-7. The time step for
675 saving the ODE output was set to be 0.1 day.

676

677 **Tracking river responses to EW using the DRN model**

678

679 For each selected river segment, we set the dissolution rate of the flood basalt
680 ($\text{Na}_{0.11}\text{K}_{0.01}\text{Fe(II)}_{0.14}\text{Mg}_{0.22}\text{Ca}_{0.22}\text{Al}_{0.38}\text{Fe(III)}_{0.05}\text{SiTi}_{0.02}\text{O}_{3.33}$) (59) in its watershed at 1 ton of basalt
681 per hectare per year in the baseline scenario. In the sensitivity tests, two additional scenarios are
682 employed: one with 0.5 ton of basalt per hectare per year and another with 1.5 tons of basalt per
683 hectare per year. This basalt mineral stoichiometries stipulate that dissolution of 1 mol of basalt is
684 equivalent to consuming 1.28 mol CO_2 from the atmosphere. Meantime, 1.28 mol DIC and 1.28
685 mol ALK (DIC:ALK = 1) along with the cations per mol of basalt dissolution, will enter the river
686 segment. Coupling the forward ODE framework (Eq. 1–4) with specified basalt dissolution rates
687 at each river segment, we track the dynamics of river chemistry (e.g., carbonate saturation state
688 and carbon degassing) in each segment of each flow path for 2 years with a time step of 0.1 day.
689 In addition to the river DIC, ALK, Ca, and salinity readily available from the ODE system, at each
690 time step, we solve the complete carbonate system chemistry using the fast numerical routine
691 proposed by Follows et al. (60), calculate the carbon degassing flux following Eq. 5 (with an
692 atmospheric CO_2 concentration of 380 ppm), and derive the calcite saturation state following Eq.
693 S1. For each flow path, we calculate the cumulative carbon degassing fluxes across the whole
694 downstream segments through time (Fig. 2B). We define the cumulative carbon leakage for each
695 flow path following Eq. S10.

696

$$697 \quad L_{\text{carbon}}(\%) = \frac{\sum_0^t (\sum_i^k F_{\text{degass_ERW}_i} - \sum_i^k F_{\text{degass_background}_i})}{\sum_0^t F_{\text{DIC}_{\text{ERW}}}} \cdot 100 \quad (\text{S10})$$

698 Where $L_{\text{carbon}}(\%)$ represents the proportion of the cumulative carbon leakage with time, t
699 represents the model time, i represents the individual segment number, k represents the number of
700 segments in the flow path, $F_{\text{degass_ERW}}$ represents the carbon degassing flux of each segment
701 following the application of EW, $F_{\text{degass_background}}$ represents the carbon degassing flux of each
702 segment before EW, and $F_{\text{DIC}_{\text{ERW}}}$ represents the DIC flux input from EW.

703

704 **Data and code availability**

705

706 The GRADES network and its associated properties (e.g., watershed area, discharge, connectivity)
707 are from here:

708 <https://www.reachhydro.org/home/params/merit-basins>

709

710 The global monthly river $p\text{CO}_2$ values can be found at the link below. The file downloaded from
711 this website is a ZIP file, which can be extracted using the default unzipping software on both
712 Windows and Mac systems.

713 <https://datadryad.org/stash/dataset/doi:10.5061/dryad.d7wm37pz9>

714 The DRN model will adhere to the GNU General Public License (GPL) standard and will be open
715 source upon acceptance of the paper.

716

717 **Acknowledgements**

718

719 The authors want to acknowledge support from the Partnership for an Advanced Computing
720 Environment (PACE) at the Georgia Institute of Technology, the Yale Center for Research
721 Computing, and the Yale Center for Natural Carbon Capture (YCNCC). Portions of this research
722 were conducted with the advanced computing resources provided by Texas A&M High
723 Performance Research Computing. SZ, NJP, and CTR acknowledge funding from the DOE Earth
724 shots award (#DE-SC0024709).

725

726 **References**

727

- 728 1. National Academies of Sciences, Engineering, and Medicine, *Negative Emissions*
729 *Technologies and Reliable Sequestration: A Research Agenda* (Washington, DC: The
730 National Academies Press, 2019) <https://doi.org/10.17226/25259> (June 16, 2021).
- 731 2. K. Riahi, *et al.*, “2022: Mitigation pathways compatible with long-term goals” in *IPCC,*
732 *2022: Climate Change 2022: Mitigation of Climate Change. Contribution of Working*
733 *Group III to the Sixth Assessment Report of the Intergovernmental Panel on Climate*
734 *Change [P. R. Shukla, J. Skea, et al., Eds. (10, 2022).*
- 735 3. J. Rogelj, *et al.*, Mitigation Pathways Compatible with 1.5°C in the Context of Sustainable
736 Development. *IPCC*, 82 (2018).
- 737 4. L. T. Bach, S. J. Gill, R. E. M. Rickaby, S. Gore, P. Renforth, CO₂ Removal With Enhanced
738 Weathering and Ocean Alkalinity Enhancement: Potential Risks and Co-benefits for Marine
739 Pelagic Ecosystems. *Front. Clim.* **1** (2019).
- 740 5. D. J. Beerling, *et al.*, Potential for large-scale CO₂ removal via enhanced rock weathering
741 with croplands. *Nature* **583**, 242–248 (2020).
- 742 6. J. Hartmann, *et al.*, Enhanced chemical weathering as a geoengineering strategy to reduce
743 atmospheric carbon dioxide, supply nutrients, and mitigate ocean acidification. *Rev.*
744 *Geophys.* **51**, 113–149 (2013).
- 745 7. Y. Kanzaki, N. J. Planavsky, C. T. Reinhard, New estimates of the storage permanence and
746 ocean co-benefits of enhanced rock weathering. *PNAS Nexus* **2**, pgad059 (2023).
- 747 8. P. Renforth, C.-L. Washbourne, J. Taylder, D. A. C. Manning, Silicate Production and
748 Availability for Mineral Carbonation. *Environ. Sci. Technol.* **45**, 2035–2041 (2011).
- 749 9. S. H. Baek, *et al.*, Impact of Climate on the Global Capacity for Enhanced Rock Weathering
750 on Croplands. *Earths Future* **11**, e2023EF003698 (2023).
- 751 10. L. L. Taylor, *et al.*, Enhanced weathering strategies for stabilizing climate and averting
752 ocean acidification. *Nat. Clim. Change* **6**, 402–406 (2016).
- 753 11. S. Zhang, *et al.*, River chemistry constraints on the carbon capture potential of surficial
754 enhanced rock weathering. *Limnol. Oceanogr.* **67**, S148–S157 (2022).
- 755 12. D. J. Beerling, *et al.*, Farming with crops and rocks to address global climate, food and soil
756 security. *Nat. Plants*, 1 (2018).
- 757 13. E. Blanc-Betes, *et al.*, In silico assessment of the potential of basalt amendments to reduce
758 N₂O emissions from bioenergy crops. *GCB Bioenergy* **13**, 224–241 (2021).
- 759 14. I. Chiaravalloti, *et al.*, Mitigation of soil nitrous oxide emissions during maize production
760 with basalt amendments. *Front. Clim.* **5** (2023).
- 761 15. W. J. Knapp, E. T. Tipper, The efficacy of enhancing carbonate weathering for carbon
762 dioxide sequestration. *Front. Clim.* **4** (2022).

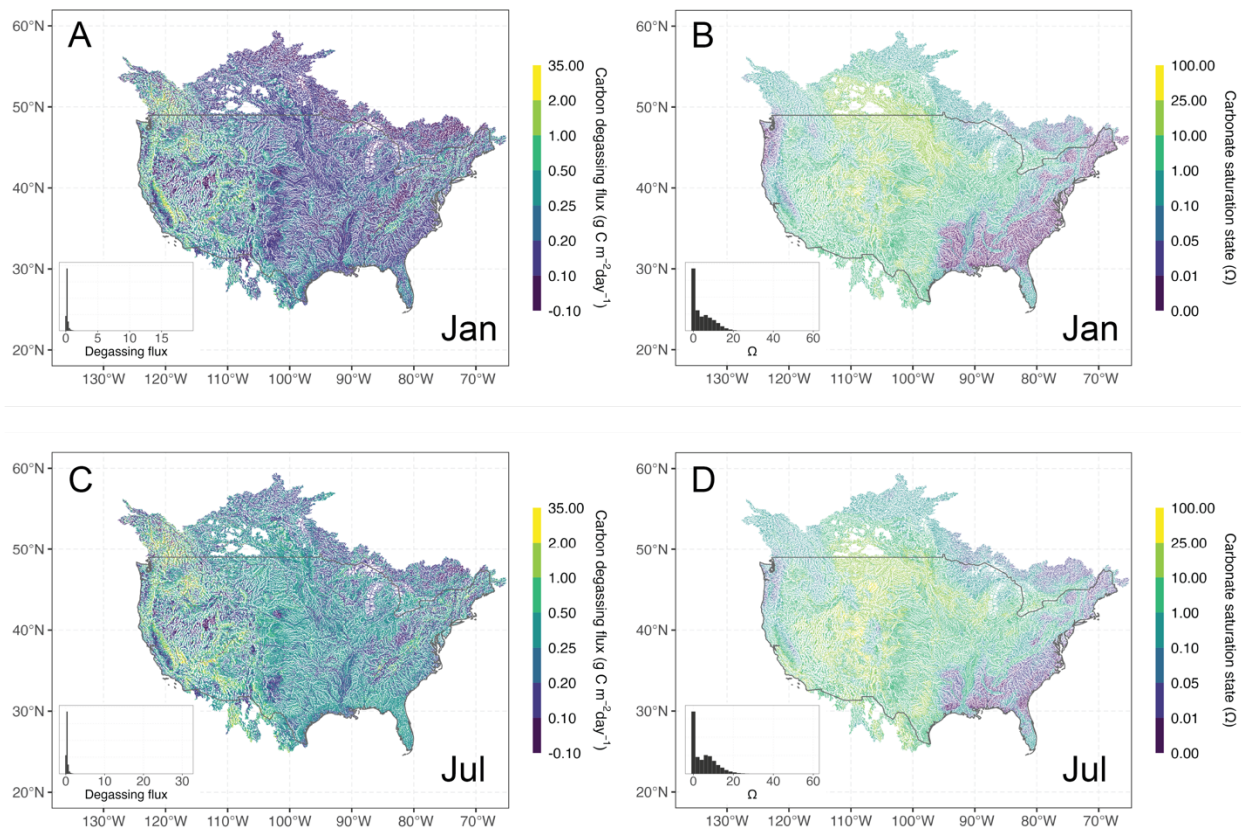
- 763 16. K. J. Harrington, R. G. Hilton, G. M. Henderson, Implications of the Riverine Response to
764 Enhanced Weathering for CO₂ removal in the UK. *Appl. Geochem.* **152**, 105643 (2023).
- 765 17. S. Liu, P. A. Raymond, Hydrologic controls on pCO₂ and CO₂ efflux in US streams and
766 rivers. *Limnol. Oceanogr. Lett.* **3**, 428–435 (2018).
- 767 18. P. Lin, *et al.*, Global Reconstruction of Naturalized River Flows at 2.94 Million Reaches.
768 *Water Resour. Res.* **55**, 6499–6516 (2019).
- 769 19. S. Liu, *et al.*, The importance of hydrology in routing terrestrial carbon to the atmosphere
770 via global streams and rivers. *Proc. Natl. Acad. Sci.* **119**, e2106322119 (2022).
- 771 20. U.S. Geological Survey, National Water Information System data available on the World
772 Wide Web (USGS Water Data for the Nation) (2016) (November 11, 2018).
- 773 21. A. J. Ulseth, *et al.*, Distinct air–water gas exchange regimes in low- and high-energy
774 streams. *Nat. Geosci.* **12**, 259–263 (2019).
- 775 22. P. A. Raymond, *et al.*, Scaling the gas transfer velocity and hydraulic geometry in streams
776 and small rivers. *Limnol. Oceanogr. Fluids Environ.* **2**, 41–53 (2012).
- 777 23. R. O. Hall Jr., A. J. Ulseth, Gas exchange in streams and rivers. *WIREs Water* **7**, e1391
778 (2020).
- 779 24. P. A. Raymond, M. B. David, J. E. Saiers, The impact of fertilization and hydrology on
780 nitrate fluxes from Mississippi watersheds. *Curr. Opin. Environ. Sustain.* **4**, 212–218
781 (2012).
- 782 25. J. Strefler, T. Amann, N. Bauer, E. Kriegler, J. Hartmann, Potential and costs of carbon
783 dioxide removal by enhanced weathering of rocks. *Environ. Res. Lett.* **13**, 034010 (2018).
- 784 26. T. Reershemius, *et al.*, Initial Validation of a Soil-Based Mass-Balance Approach for
785 Empirical Monitoring of Enhanced Rock Weathering Rates. *Environ. Sci. Technol.* **57**,
786 19497–19507 (2023).
- 787 27. C. Neal, Calcite saturation in eastern UK rivers. *Sci. Total Environ.* **282–283**, 311–326
788 (2002).
- 789 28. D. L. Suarez, Calcite supersaturation and precipitation kinetics in the Lower Colorado
790 River, All-American Canal and East Highline Canal. *Water Resour. Res.* **19**, 653–661
791 (1983).
- 792 29. K. Szramek, L. M. Walter, Impact of Carbonate Precipitation on Riverine Inorganic Carbon
793 Mass Transport from a Mid-continent, Forested Watershed. *Aquat. Geochem.* **10**, 99–137
794 (2004).
- 795 30. K. S. Aho, P. A. Raymond, Differential Response of Greenhouse Gas Evasion to Storms in
796 Forested and Wetland Streams. *J. Geophys. Res. Biogeosciences* **124**, 649–662 (2019).
- 797 31. J. D. Schade, J. Bailio, W. H. McDowell, Greenhouse gas flux from headwater streams in
798 New Hampshire, USA: Patterns and drivers. *Limnol. Oceanogr.* **61**, S165–S174 (2016).
- 799 32. B. Lehner, G. Grill, Global river hydrography and network routing: baseline data and new
800 approaches to study the world’s large river systems. *Hydrol. Process.* **27**, 2171–2186
801 (2013).
- 802 33. S. A. Comer-Warner, *et al.*, Thermal sensitivity of CO₂ and CH₄ emissions varies with
803 streambed sediment properties. *Nat. Commun.* **9**, 2803 (2018).
- 804 34. P. Romeijn, S. A. Comer-Warner, S. Ullah, D. M. Hannah, S. Krause, Streambed Organic
805 Matter Controls on Carbon Dioxide and Methane Emissions from Streams. *Environ. Sci.*
806 *Technol.* **53**, 2364–2374 (2019).
- 807 35. P. Renforth, G. Henderson, Assessing ocean alkalinity for carbon sequestration. *Rev.*
808 *Geophys.* **55**, 636–674 (2017).

- 809 36. T. Maavara, *et al.*, Watershed DOC uptake occurs mostly in lakes in the summer and in
810 rivers in the winter. *Limnol. Oceanogr.* **68**, 735–751 (2023).
- 811 37. S. Wang, *et al.*, The community-centered freshwater biogeochemistry model unified RIVE
812 v1.0: a unified version for water column. *Geosci. Model Dev.* **17**, 449–476 (2024).
- 813 38. E. S. Bernhardt, *et al.*, The metabolic regimes of flowing waters. *Limnol. Oceanogr.* **63**,
814 S99–S118 (2018).
- 815 39. J.-P. Gattuso, J.-M. Epitalon, H. Lavigne, J. Orr, Seawater Carbonate Chemistry [R package
816 seacarb version 3.2.16] (2021) (May 28, 2021).
- 817 40. R. E. Zeebe, D. Wolf-Gladrow, *CO₂ in seawater: Equilibrium, kinetics, isotopes*, Volume
818 65, 1 edition (Elsevier Science, 2001).
- 819 41. P. A. Raymond, *et al.*, Global carbon dioxide emissions from inland waters. *Nature* **503**,
820 355–359 (2013).
- 821 42. D. N. Karger, *et al.*, Climatologies at high resolution for the earth’s land surface areas. *Sci.*
822 *Data* **4**, 170122 (2017).
- 823 43. G. Ghiggi, V. Humphrey, S. I. Seneviratne, L. Gudmundsson, G-RUN ENSEMBLE: A
824 Multi-Forcing Observation-Based Global Runoff Reanalysis. *Water Resour. Res.* **57**,
825 e2020WR028787 (2021).
- 826 44. Y. Wang, *et al.*, Development of observation-based global multilayer soil moisture products
827 for 1970 to 2016. *Earth Syst. Sci. Data* **13**, 4385–4405 (2021).
- 828 45. J. Hartmann, N. Moosdorf, The new global lithological map database GLiM: A
829 representation of rock properties at the Earth surface. *Geochem. Geophys. Geosystems* **13**,
830 Q12004 (2012).
- 831 46. M.-N. Tuanmu, W. Jetz, A global 1-km consensus land-cover product for biodiversity and
832 ecosystem modelling. *Glob. Ecol. Biogeogr.* **23**, 1031–1045 (2014).
- 833 47. G. Amatulli, D. McNerney, T. Sethi, P. Strobl, S. Domisch, Geomorpho90m, empirical
834 evaluation and accuracy assessment of global high-resolution geomorphometric layers. *Sci.*
835 *Data* **7**, 162 (2020).
- 836 48. I. J. Larsen, D. R. Montgomery, H. M. Greenberg, The contribution of mountains to global
837 denudation. *Geology* **42**, 527–530 (2014).
- 838 49. L. Poggio, *et al.*, SoilGrids 2.0: producing soil information for the globe with quantified
839 spatial uncertainty. *SOIL* **7**, 217–240 (2021).
- 840 50. M. Zhao, F. A. Heinsch, R. R. Nemani, S. W. Running, Improvements of the MODIS
841 terrestrial gross and net primary production global data set. *Remote Sens. Environ.* **95**, 164–
842 176 (2005).
- 843 51. B. Pan, S. K. Lam, E. Wang, A. Mosier, D. Chen, New approach for predicting nitrification
844 and its fraction of N₂O emissions in global terrestrial ecosystems. *Environ. Res. Lett.* **16**,
845 034053 (2021).
- 846 52. L. Breiman, Random Forests. *Mach. Lang.* **45**, 5–32 (2001).
- 847 53. T. Hastie, R. Tibshirani, J. Friedman, *The elements of statistical learning: Data mining,*
848 *inference, and prediction, second edition*, 2nd edition (Springer, 2016).
- 849 54. B. E. S. Zhang, C. T. Driscoll, T. Wen, Human and natural impacts on the U.S. freshwater
850 salinization and alkalization: A machine learning approach. *Sci. Total Environ.* **889**,
851 164138 (2023).
- 852 55. R Core Team, R: A language and environment for statistical computing. *R Found. Stat.*
853 *Comput. Vienna Austria HttpswwwR-Proj.* (2017).

- 854 56. M. N. Wright, A. Ziegler, ranger: A Fast Implementation of Random Forests for High
855 Dimensional Data in C++ and R. *J. Stat. Softw.* **77**, 1–17 (2017).
- 856 57. F. N. Fritsch, R. E. Carlson, Monotone Piecewise Cubic Interpolation. *SIAM J. Numer.*
857 *Anal.* **17**, 238–246 (1980).
- 858 58. K. Soetaert, T. Petzoldt, R. W. Setzer, Solving Differential Equations in R: Package
859 deSolve. *J. Stat. Softw.* **33**, 1–25 (2010).
- 860 59. L. Marini, *Geological Sequestration of Carbon Dioxide: Thermodynamics, Kinetics, and*
861 *Reaction Path Modeling*, 1st edition (Elsevier Science, 2006).
- 862 60. M. J. Follows, T. Ito, S. Dutkiewicz, On the solution of the carbonate chemistry system in
863 ocean biogeochemistry models. *Ocean Model.* **12**, 290–301 (2006).

864
865
866
867
868
869
870
871
872
873
874
875
876
877
878
879
880
881
882
883
884
885
886
887
888
889
890
891
892

Figures



893

894 **Figure 1.** Predicted background carbon degassing flux and carbonate mineral (calcite) saturation
 895 state (Ω) for each river segment across the North America river network. (A) Carbon degassing
 896 flux in January (B) River Ω values in January (C) Carbon degassing flux in July (D) River Ω values
 897 in July. The lines represent the river segments within North America.

898

899

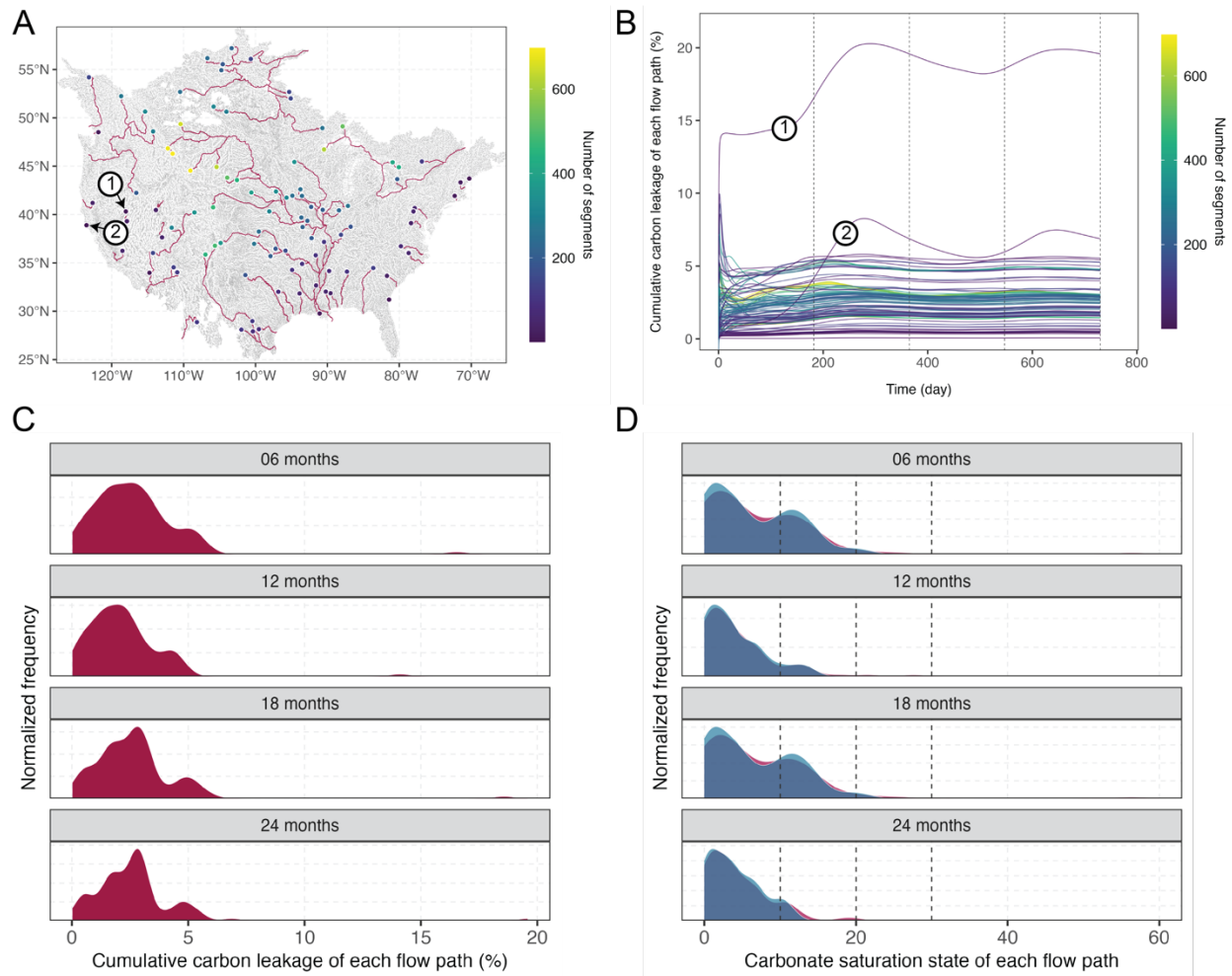
900

901

902

903

904



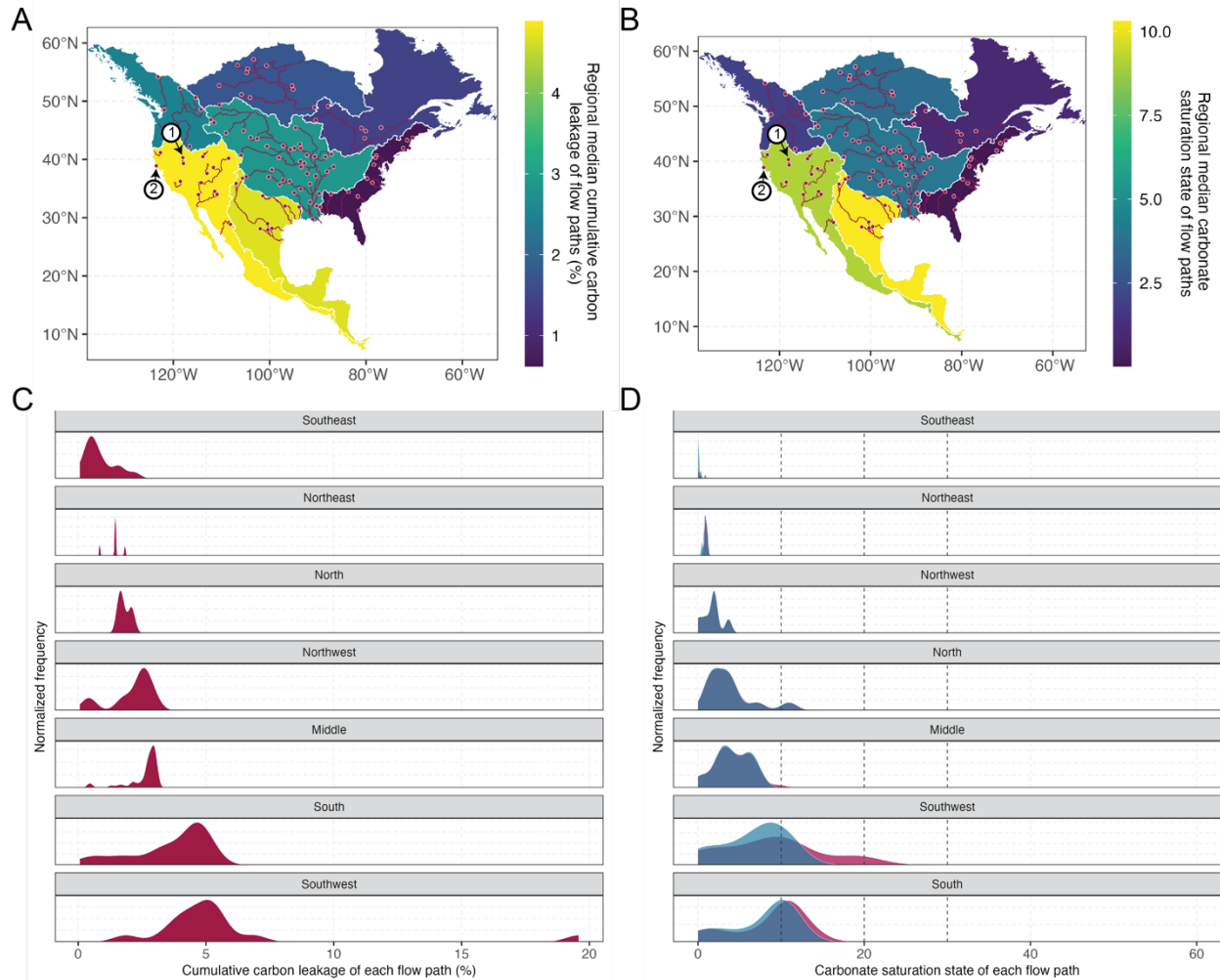
905

906 **Figure 2.** Changes in cumulative carbon leakage rate and carbonate mineral (calcite) saturation
 907 state in the downstream in response to the incoming EW fluxes in North American watersheds. (A)
 908 EW application sites (100 random sites) and their corresponding downstream segments. (B)
 909 Cumulative carbon leakage rate through time across the whole downstream segments of each flow
 910 path for each EW application site. (C) Frequency distribution of the cumulative carbon leakage of
 911 the whole flow path through time. (D) Frequency distribution of median carbonate saturation state
 912 of river segments for each flow path through time. The two symbols (1 and 2) in panel A and B
 913 represent the two flow paths with the highest leakage rates. Dashed lines in panel B represent
 914 Ω values of 10, 20, and 30 from left to right. Dashed lines in panel D represent
 915 conditions prior to EW application, while red distributions represent conditions after EW application.

917

918

919



920
 921 **Figure 3.** Spatial differences in river network responses to incoming EW fluxes in the North
 922 America watersheds. (A) Median cumulative carbon leakage of the whole flow path in each region
 923 after 24 months. (B) Median carbonate mineral (calcite) saturation state of all river segments in
 924 each region after 24 months. (C) Frequency distribution of the cumulative carbon leakage of the
 925 whole flow path in each region after 24 months. (D) Frequency distribution of carbonate saturation
 926 state of all flow paths in each region after 24 months. The two symbols (1 and 2) in panel A and
 927 B represent the two flow paths with the highest leakage rates. Dashed lines in panel D represent Ω
 928 values of 10, 20, and 30 from left to right. Blue distributions in panel D indicate conditions prior
 929 to EW application, while red distributions represent conditions after EW application.

930
 931

1 **Supporting Information for**

2
3 **Constraining carbon loss from rivers following terrestrial enhanced rock weathering**

4
5 Shuang Zhang^{a,1}, Christopher T. Reinhard^b, Shaoda Liu^c, Yoshiki Kanzaki^b, Noah J. Planavsky^{d,e}

6
7 ^aDepartment of Oceanography, Texas A&M University, College Station, TX, USA

8 ^bSchool of Earth and Atmospheric Sciences, Georgia Institute of Technology, Atlanta, GA, USA

9 ^cSchool of Environment, Beijing Normal University, Beijing, China

10 ^dDepartment of Earth and Planetary Sciences, Yale University, New Haven, CT, USA

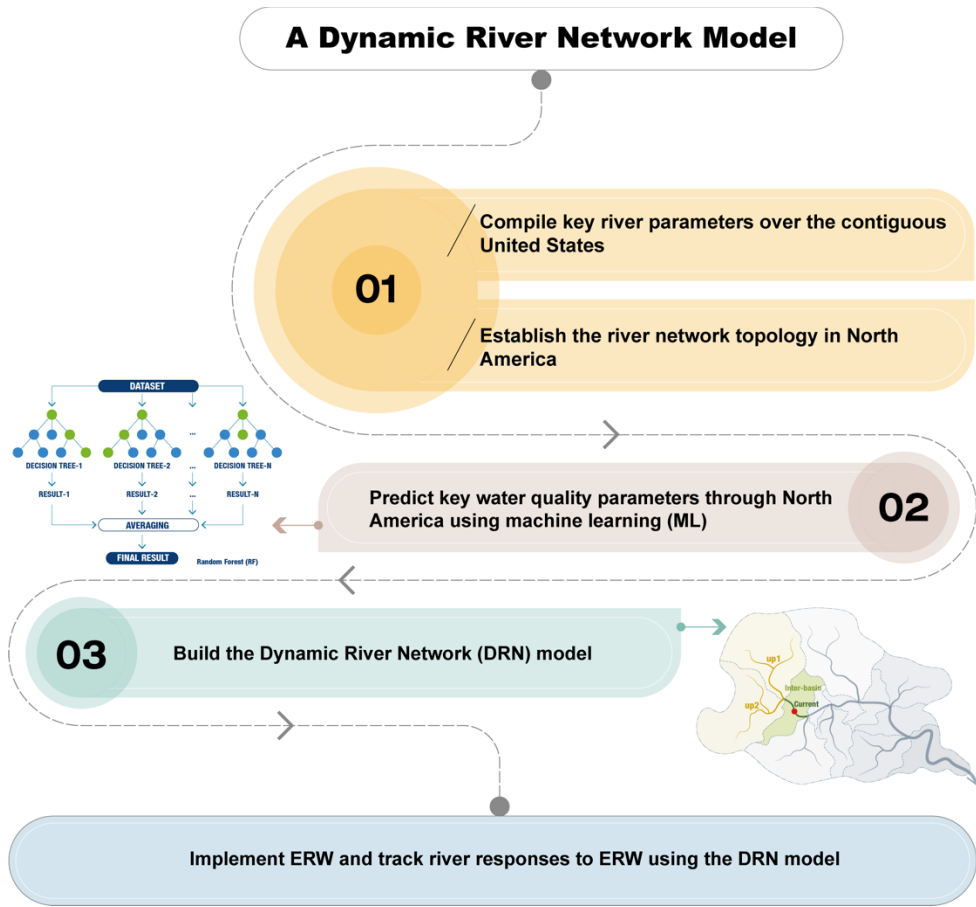
11 ^eYale Center for Natural Carbon Capture, Yale University, New Haven, CT, USA

12
13 ***Corresponding author:** Shuang Zhang

14 **Email:** shuang-zhang@tamu.edu

15
16
17 **This PDF file includes:**

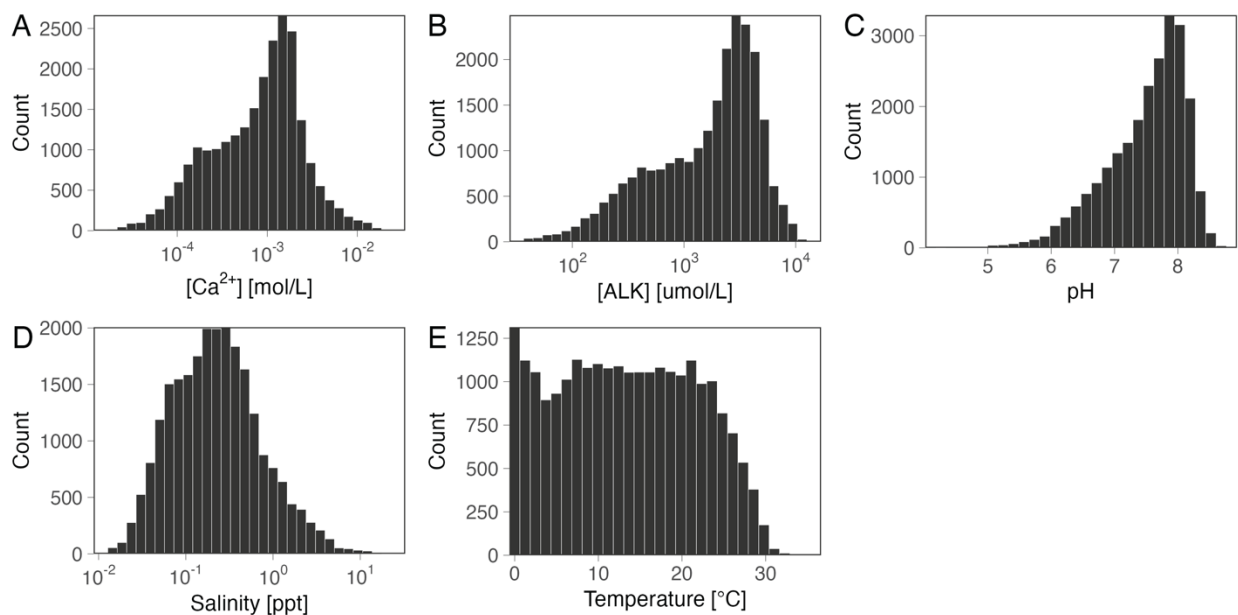
18
19 Figures S1 to S21



44
45
46
47

Figure S1. The workflow of building the dynamic river network model.

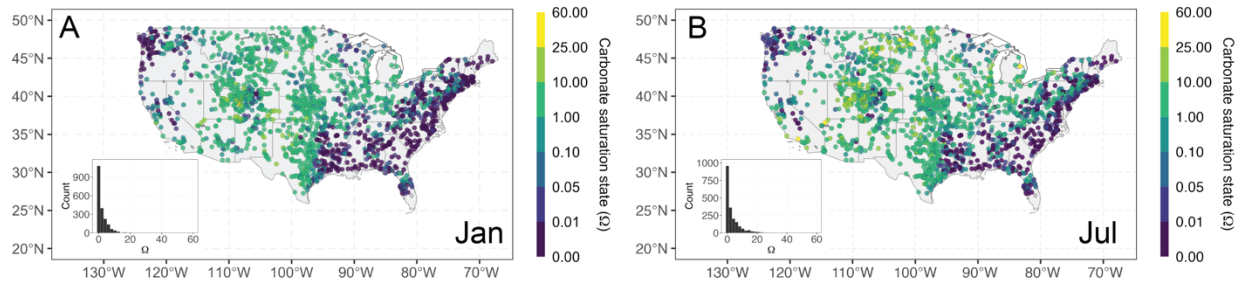
48



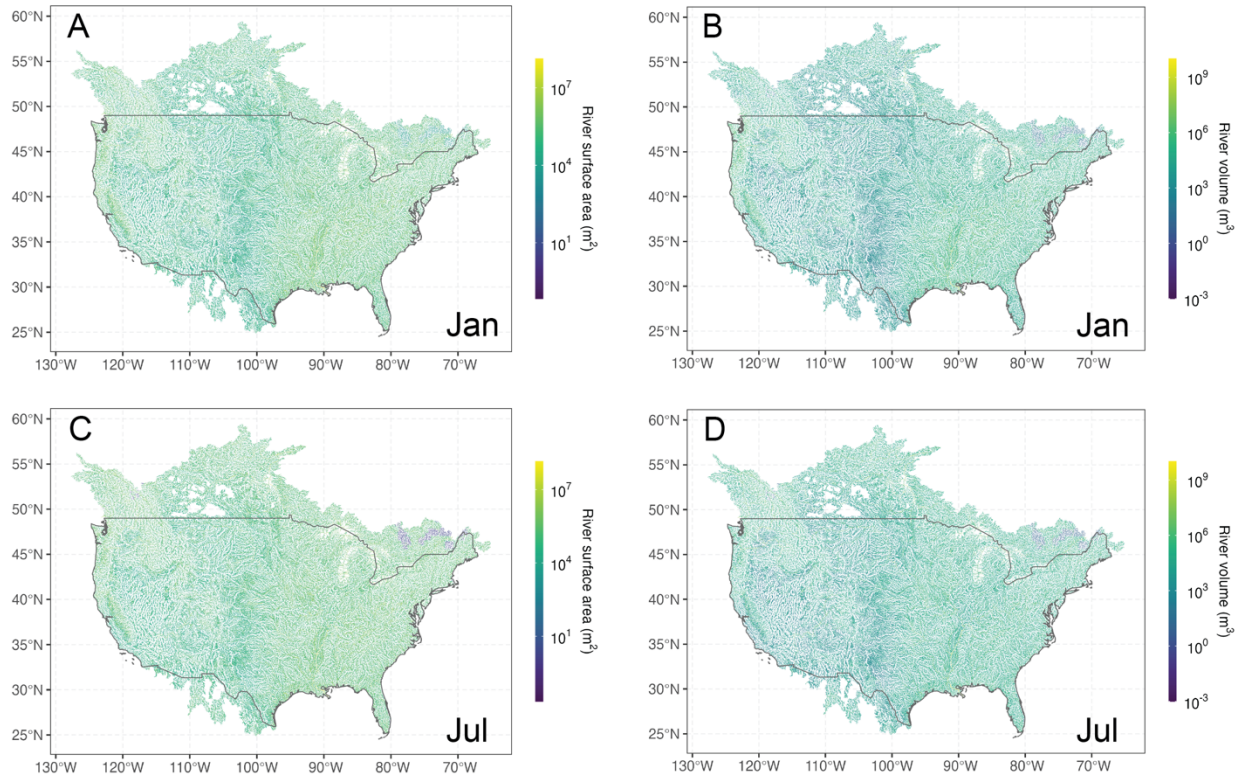
49

50

51 **Figure S2.** Frequency distributions of collected solute, salinity, and temperature data from
52 USGS for river data in the U.S. Shown are the key parameters for solving the carbonate system,
53 including (A) dissolved Ca^{2+} , (B) ALK, (C) pH, (D) salinity, and (E) temperature.

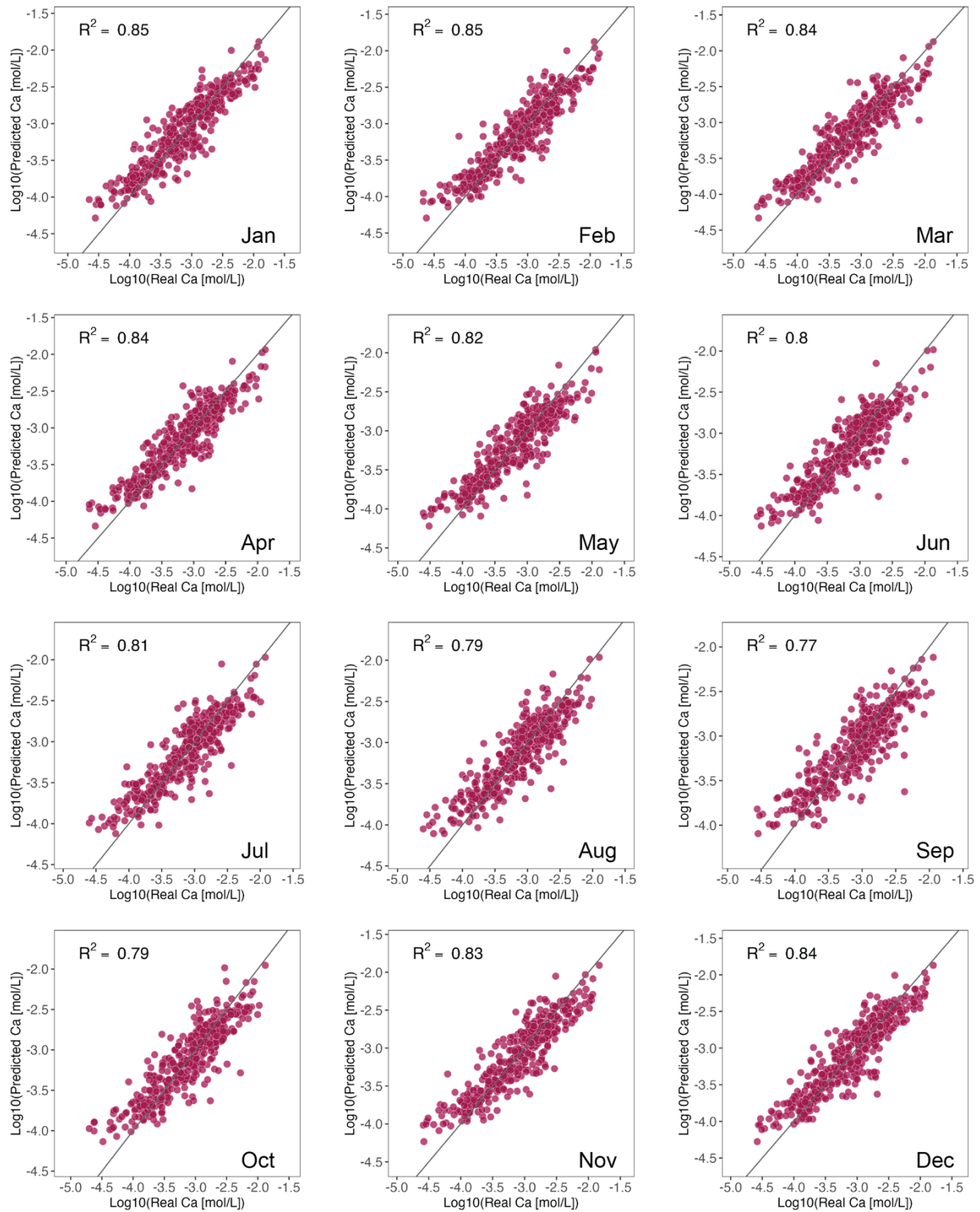


54
 55 **Figure S3.** River site locations and distributions of calcite saturation state (Ω) in January (A) and
 56 July (B) across the coterminous U.S.
 57



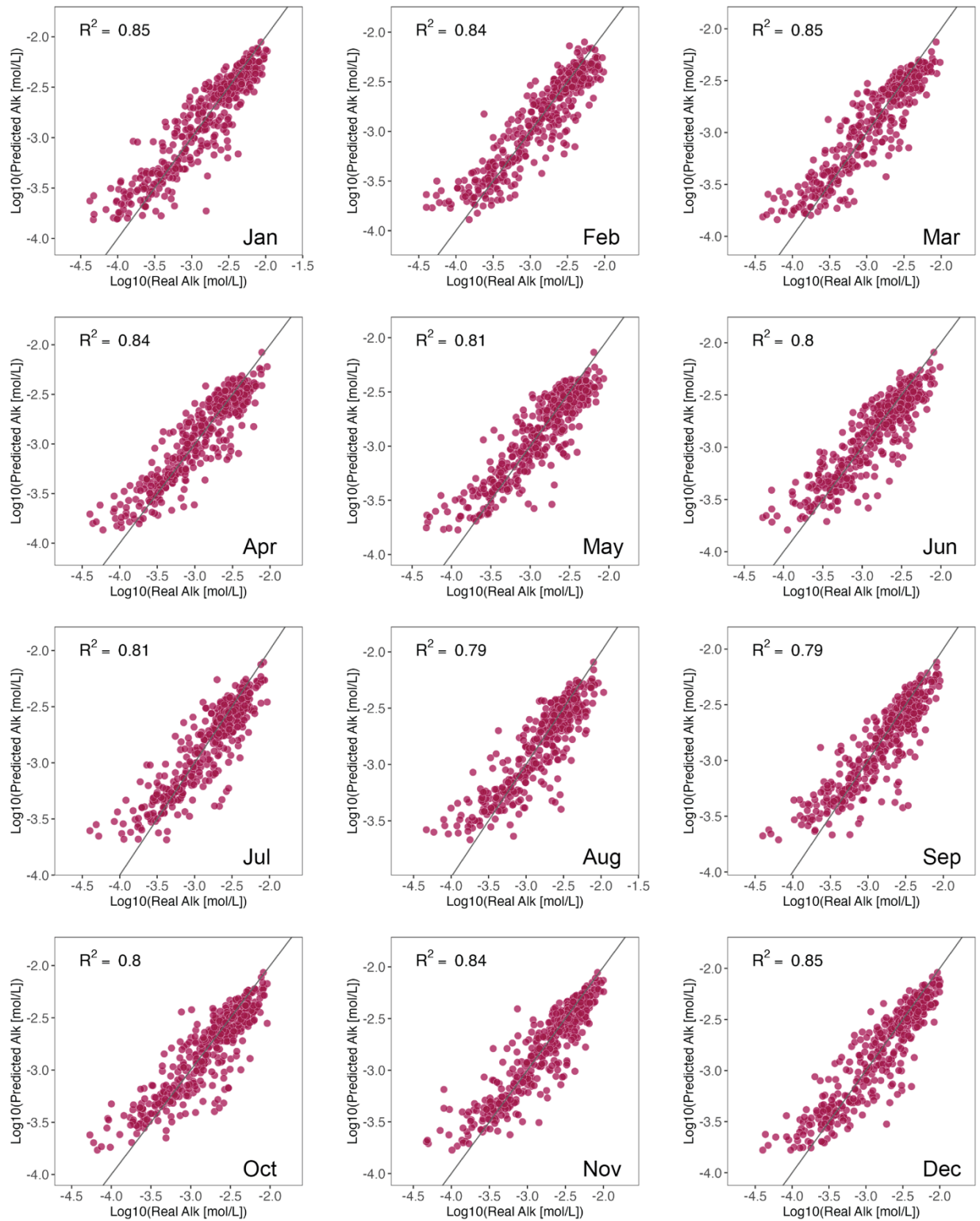
58
59
60
61
62

Figure S4. Reconstructed River segment surface area and volume from the GRADES database for January and July.

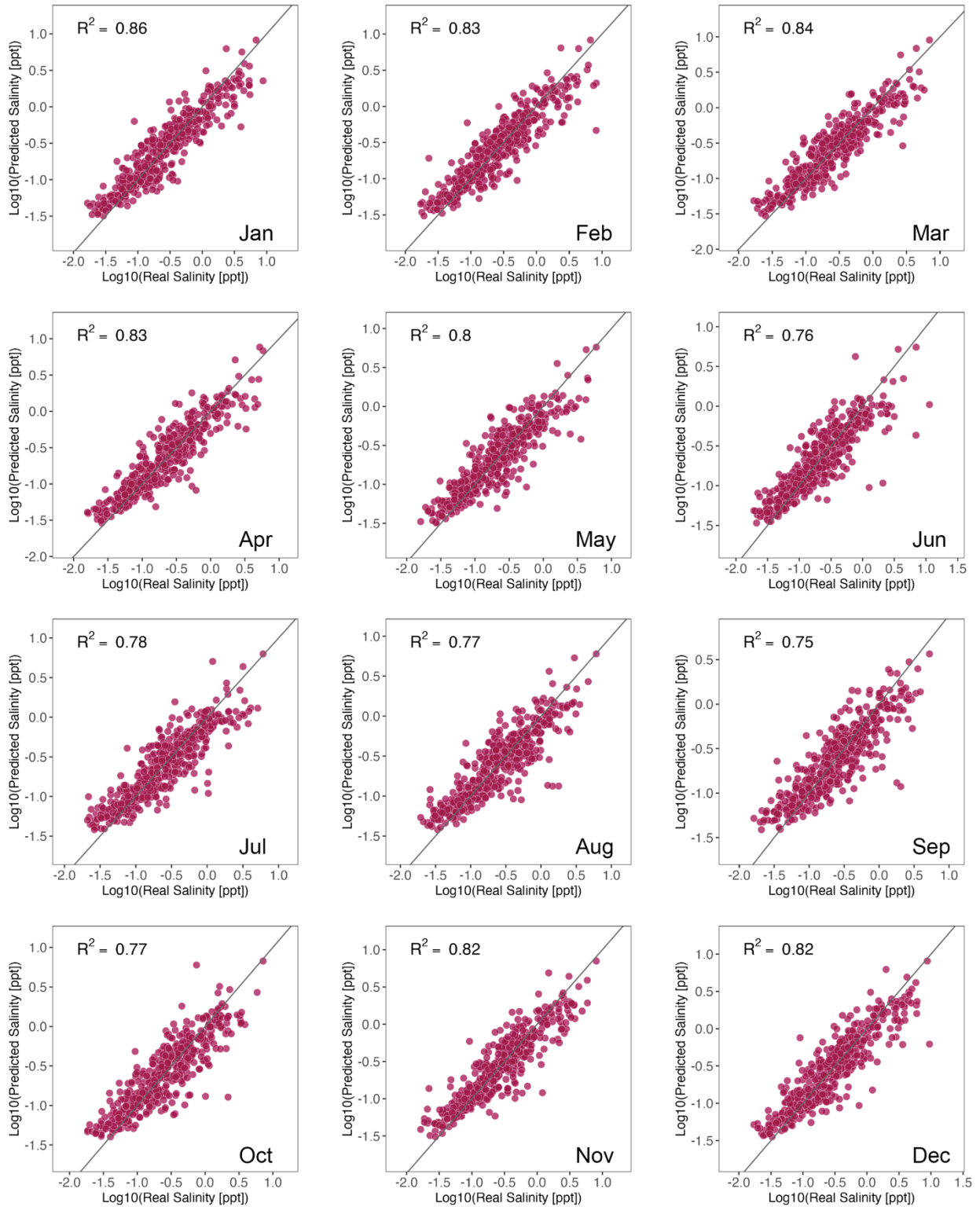


63
64
65
66
67

Figure S5. The correspondence of ML-predicted Ca concentration and the real Ca concentration for the test dataset at each month.

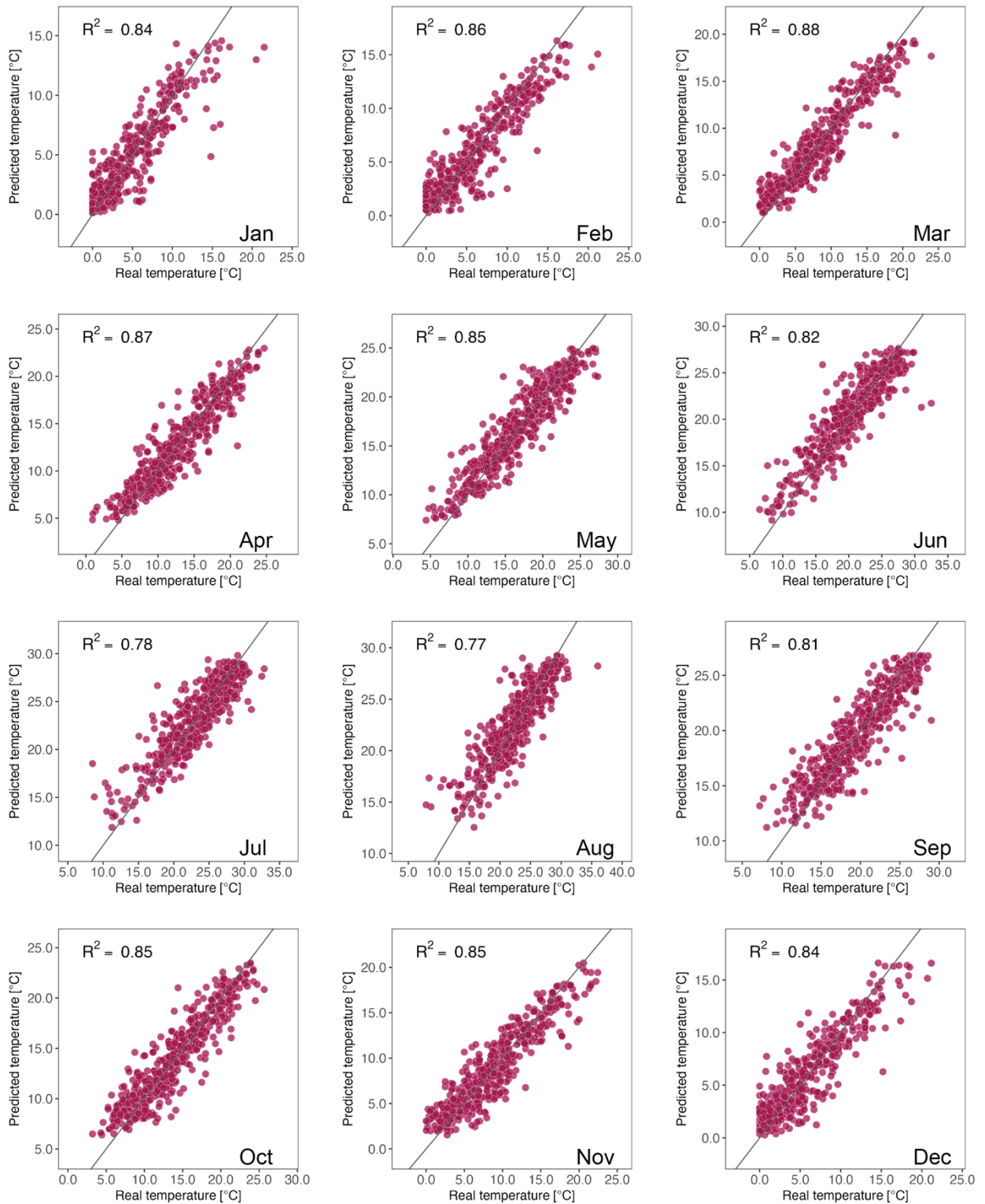


68
 69 **Figure S6.** The correspondence of ML-predicted ALK and the real ALK for the test dataset at
 70 each month.
 71
 72



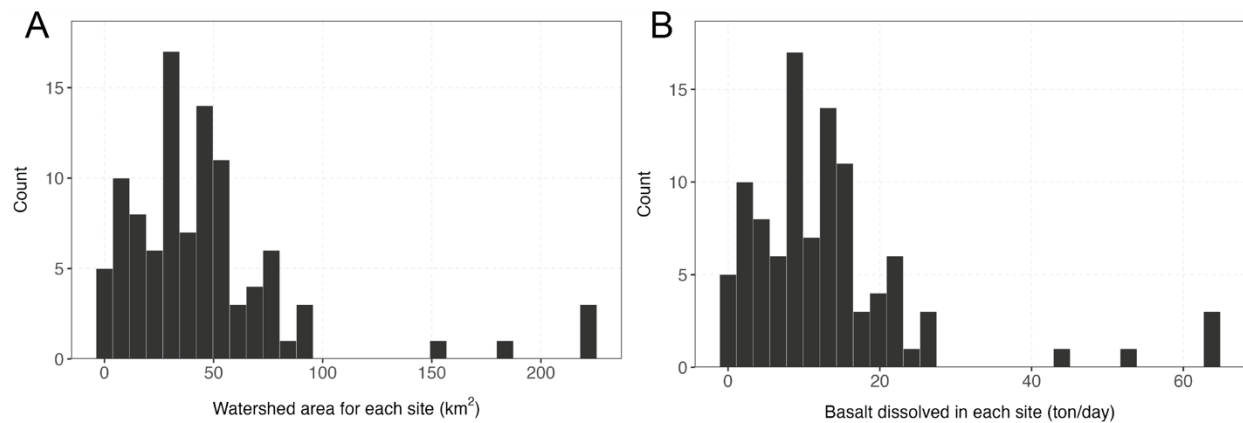
73
74
75
76
77

Figure S7. The correspondence of ML-predicted salinity and the real salinity for the test dataset at each month.



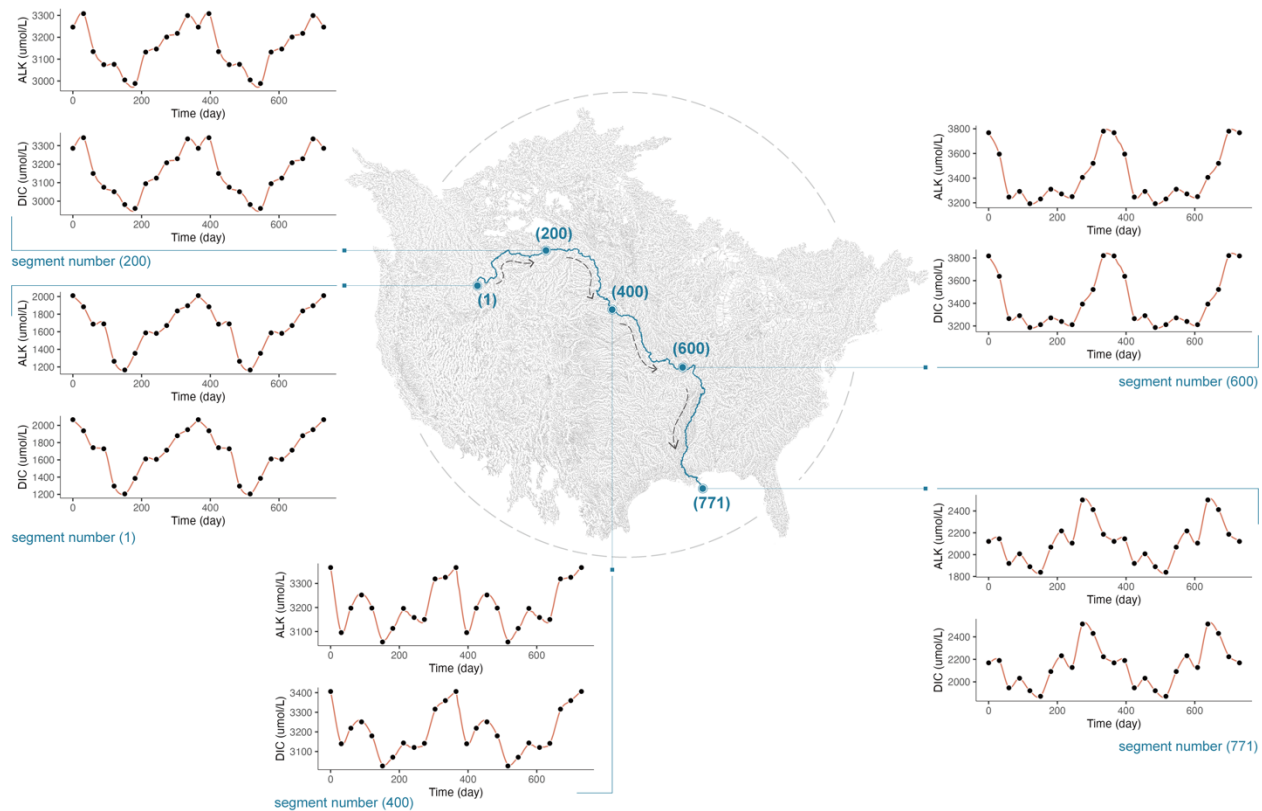
78
79
80
81
82

Figure S8. The correspondence of ML-predicted water temperature and the real water temperature for the test dataset at each month.

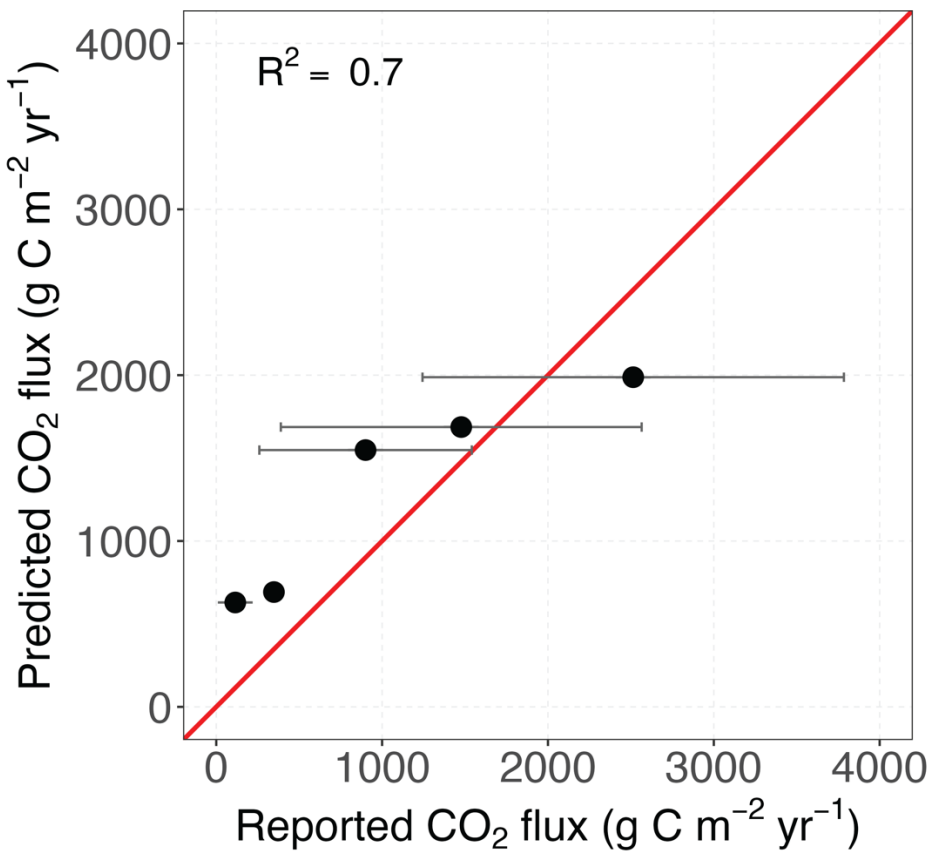


83
84
85
86
87

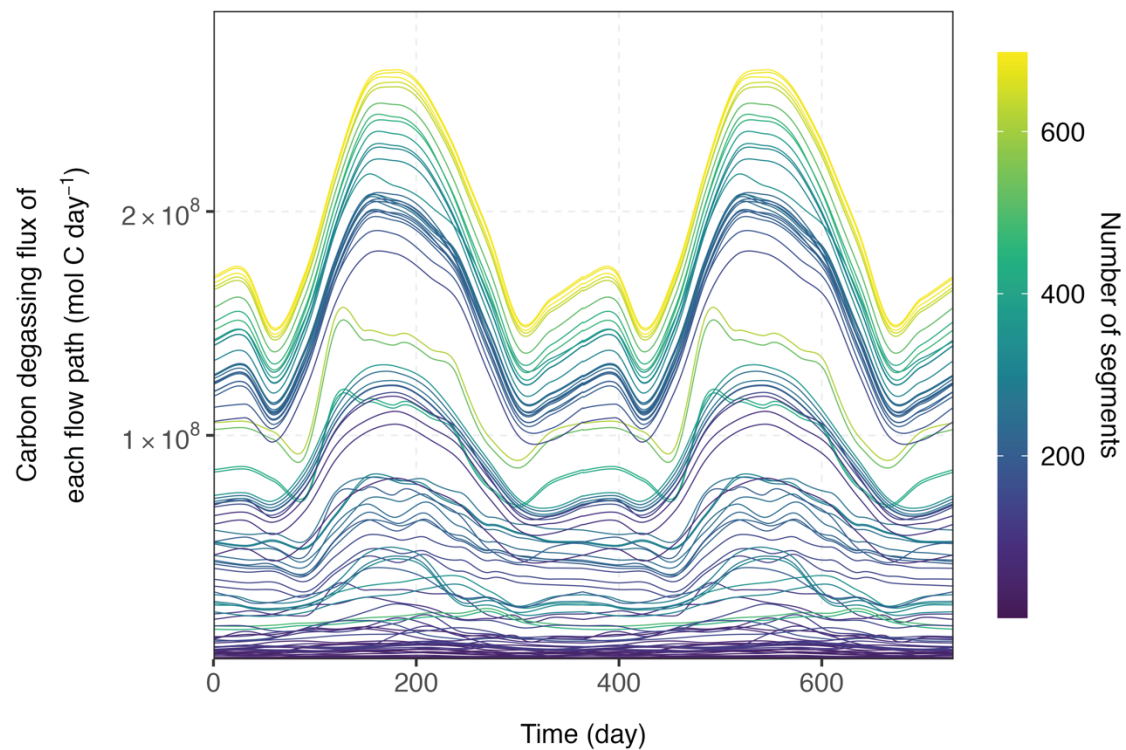
Figure S9. Watershed areas of the headwater segment (A) and basalt dissolution rate (B) for the 100 application sites across North America.



88
 89 **Figure S10.** DRN model reconstruction of background chemistry of the Mississippi River. From
 90 top to bottom on the map, the river segment numbers are 1 (the headwater), 200, 400, 600, and
 91 771 (the Mississippi river outlet) sequentially. Background monthly river chemistry (DIC and
 92 ALK) is represented by the black dots and the model simulation result is represented by the red
 93 line.
 94

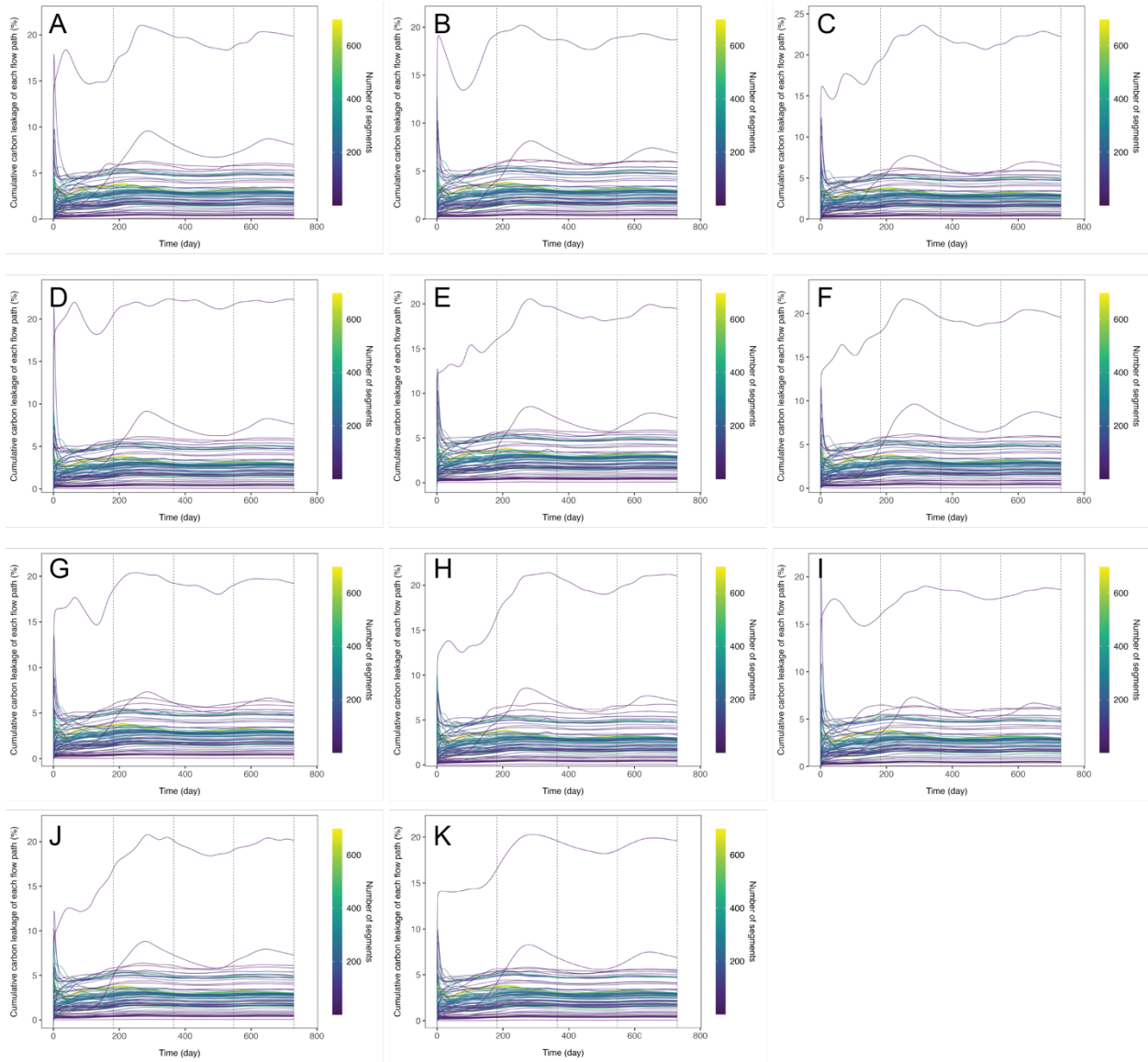


95
 96 **Fig S11.** Comparing predicted CO₂ degassing per water surface area with values reported in the
 97 literature. The reported values are for the rivers in central Connecticut and New Hampshire
 98 (references can be found in the main text). We matched the river sites mentioned in the literature
 99 with the nearest river segments in our model. Then, we compared the average monthly or annual
 100 carbon degassing flux (as resolved by the reports) of the sites located on the same river segment
 101 with our model's outcomes. The error bar represents 1 standard deviation of the reported carbon
 102 degassing across multiple sites that are snapped to the same river segment.



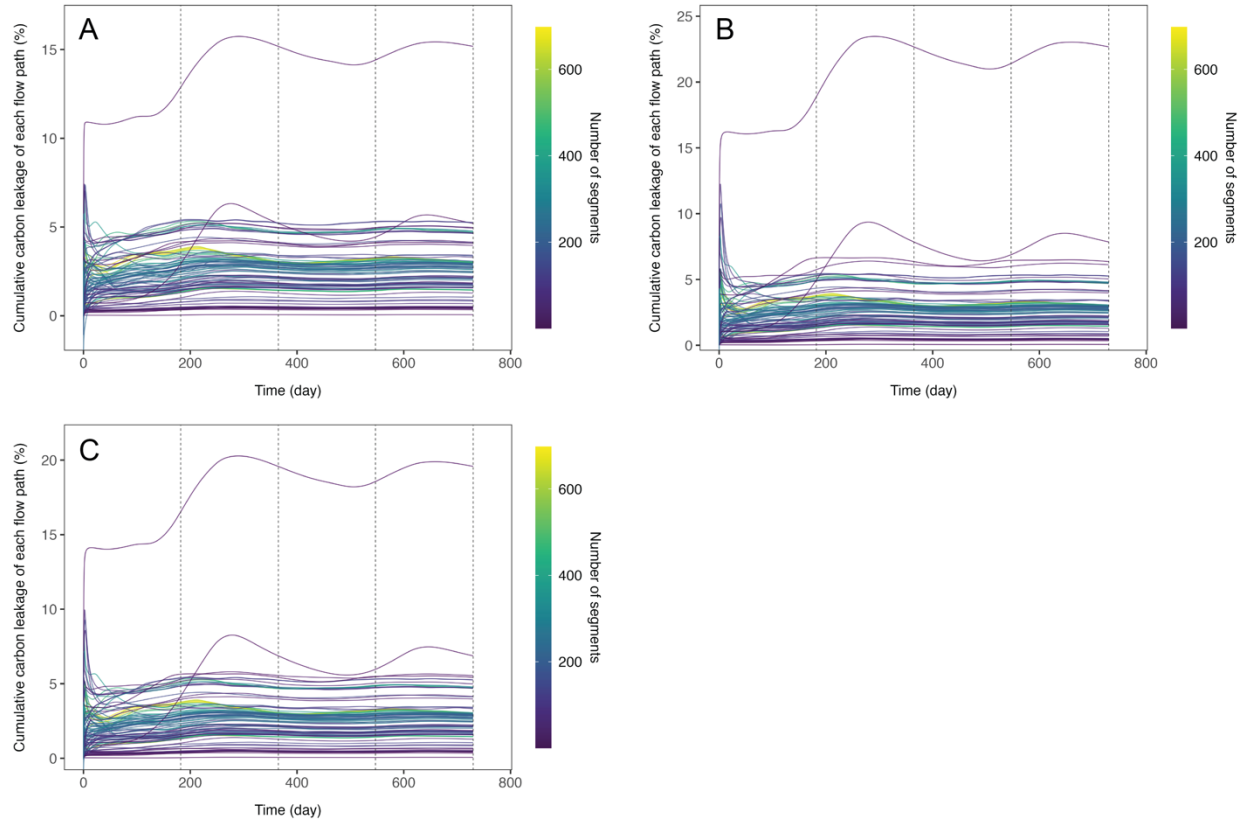
103
104
105
106
107

Figure S12. Carbon degassing flux through time across the whole downstream segments of each flow path for the 100 ERW application sites.



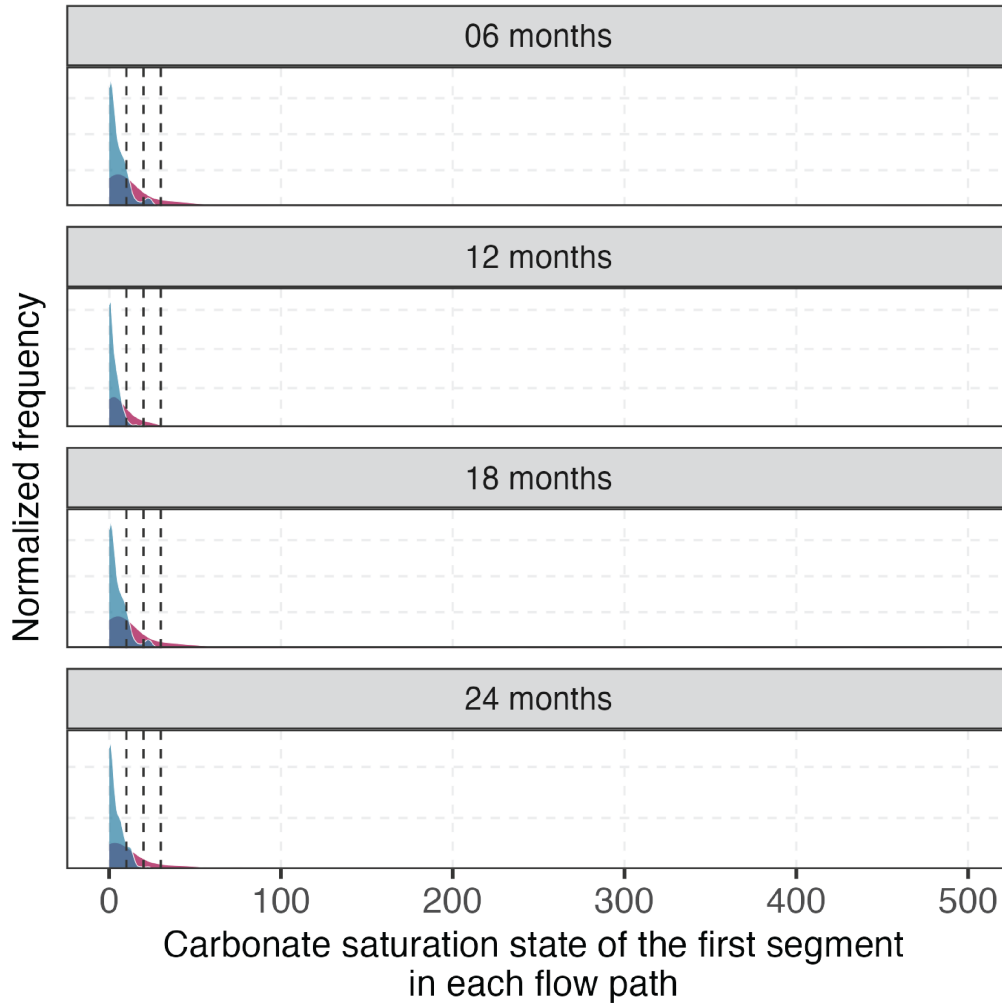
108
 109
 110
 111
 112
 113
 114

Figure S13. Sensitivity tests of the cumulative carbon leakage rate through time across the whole downstream segments of each flow path for each ERW application site. (A-J) The 10 sensitivity test results. (K) The baseline results. Note that the baseline results are shown here for comparison with the sensitivity test results.



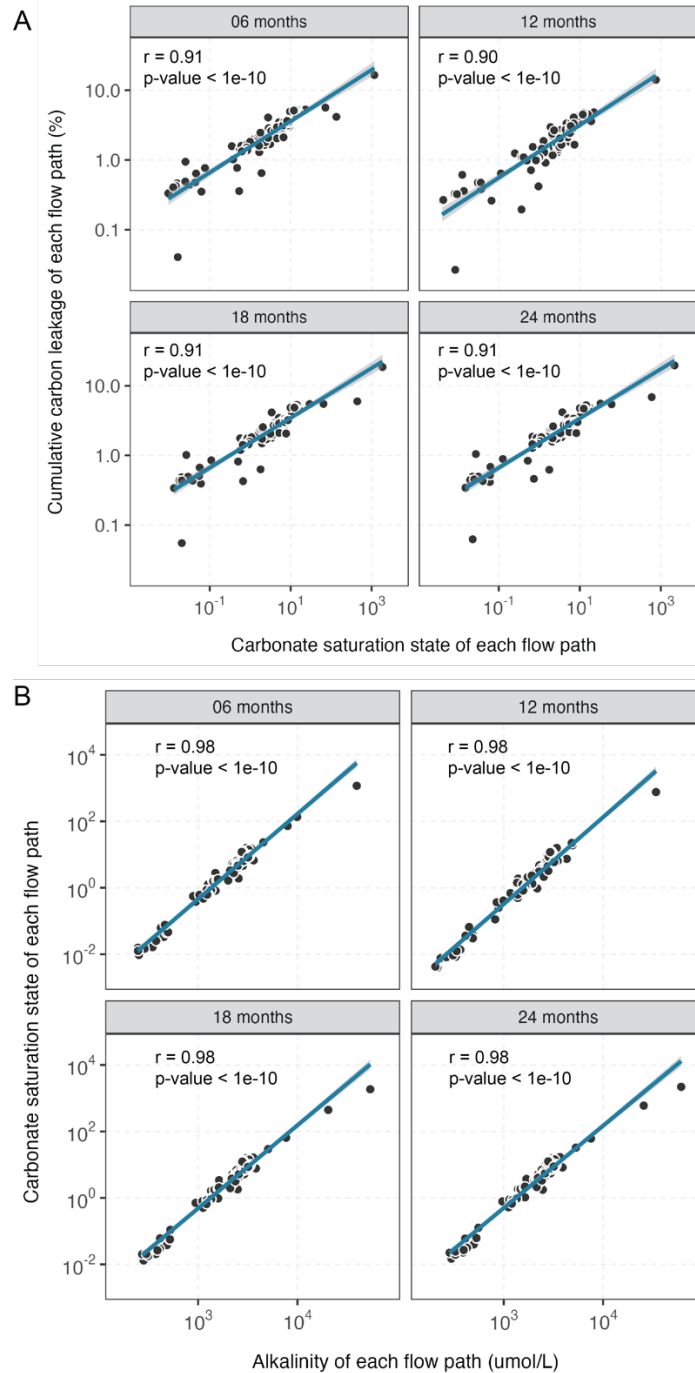
115
 116
 117
 118
 119
 120
 121
 122
 123

Figure S14. Different scenarios (low, high, and baseline) of the cumulative carbon leakage rate through time across the whole downstream segments of each flow path for each ERW application site. (A) The low scenario with 0.5 ton of basalt dissolution per hectare per year. (B) The high scenario with 1.5 ton of basalt dissolution per hectare per year. (C) The baseline scenario with 1 ton of basalt dissolution per hectare per year. Note that the baseline scenario is shown here for comparison with the other two scenarios.



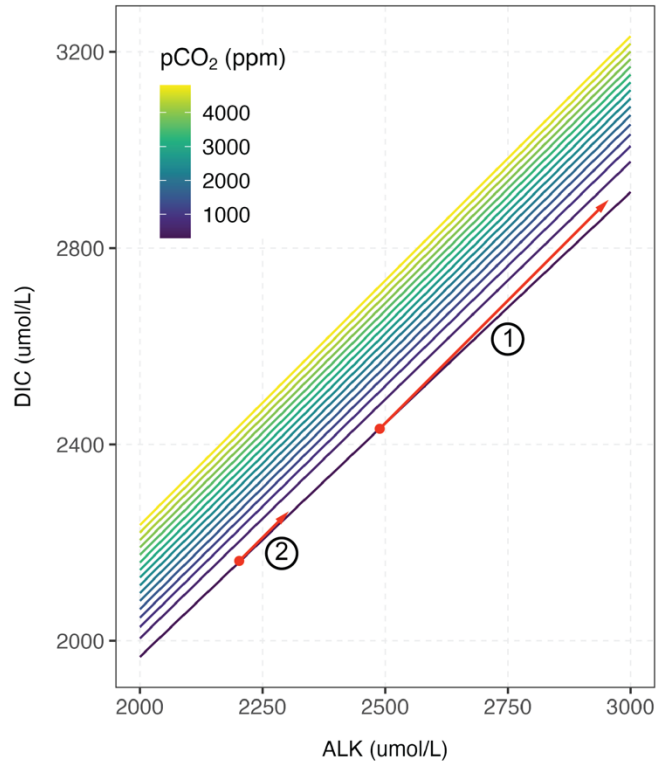
124
 125 **Figure S15.** Frequency distribution of carbonate saturation state of the first river segment for each
 126 flow path through time. Dashed lines represent Ω values of 10, 20, and 30 from left to right. Blue
 127 distributions indicate conditions prior to EW application, while red distributions represent
 128 conditions after EW application. As the distribution of Ω values is extremely right-skewed,
 129 extreme Ω values bigger than 200 (~10% of the data) are not plotted to help visualization.

130
 131
 132
 133



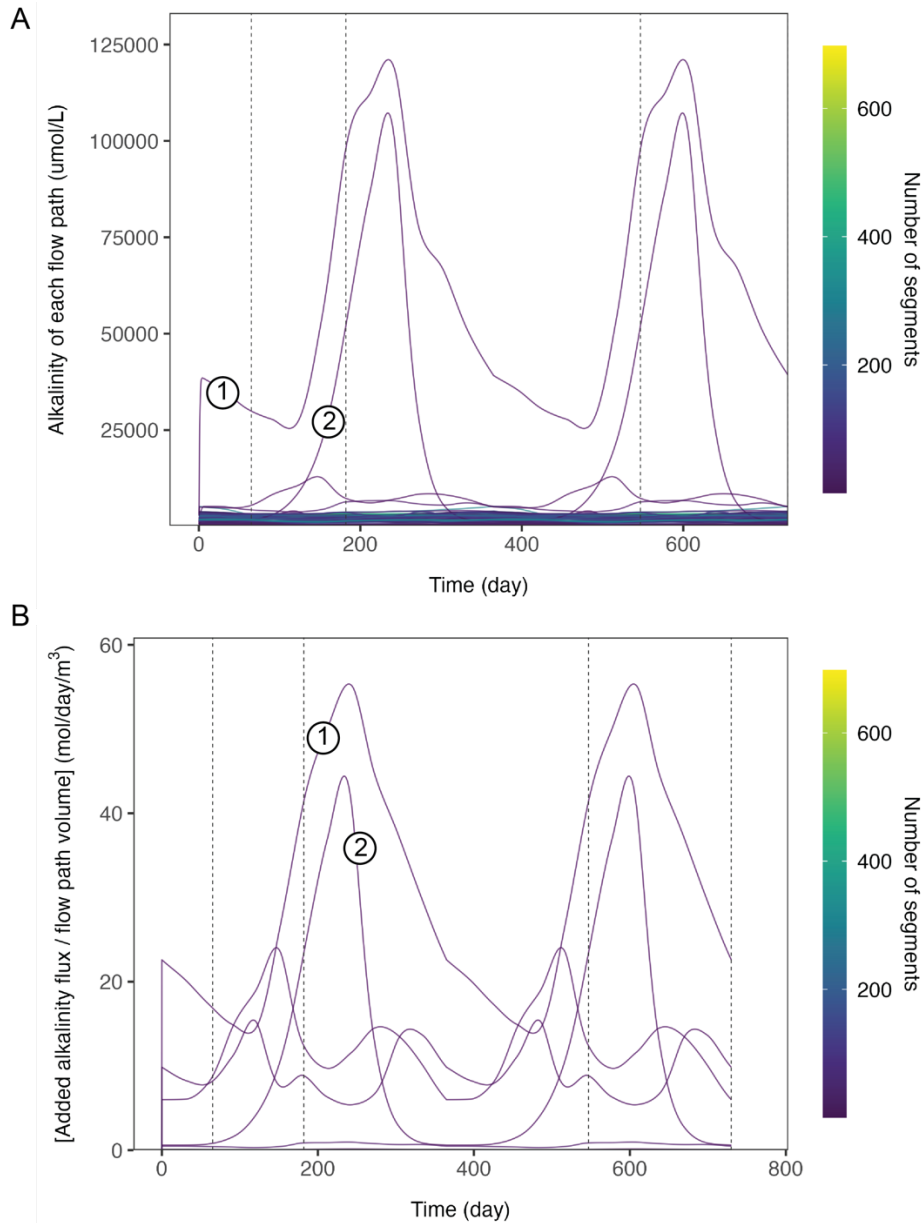
134
 135
 136
 137
 138
 139
 140
 141
 142
 143

Figure S16. Correlation between the cumulative carbon leakage rate, the median carbonate saturation state, and the median alkalinity of segments for each flow path over durations of 6, 12, 18, and 24 months. Here, the carbonate saturation state represents the average of the median carbonate saturation states of segments for each flow path from day 0 to the specified duration. The alkalinity represents the average of the median alkalinity of segments for each flow path from day 0 to the specified duration. The correlation coefficient (r) and the p -value are also shown.



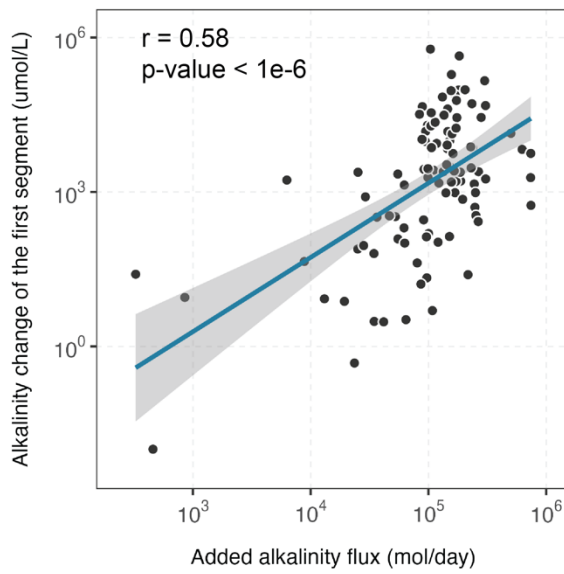
144
 145
 146
 147
 148
 149
 150
 151
 152
 153
 154

Figure S17. Thermodynamic relations of alkalinity (ALK), total dissolved inorganic carbon (DIC) and the equilibrium $p\text{CO}_2$ in river (μatm) plotted for salinity=1 and temperature=12°C. The contour lines depict the correlation between ALK and DIC for individual $p\text{CO}_2$ values ranging from 300 to 5000 μatm , a range typical for the river systems in North America. The two red arrows in panel b illustrate the input of DIC and ALK at a 1:1 ratio into the river. The length of the arrow represents the quantity of DIC and ALK introduced into the river. A longer arrow, denoted by symbol 1, signifies a larger input flux and an associated greater increase in $p\text{CO}_2$ than a shorter arrow, represented by symbol 2.

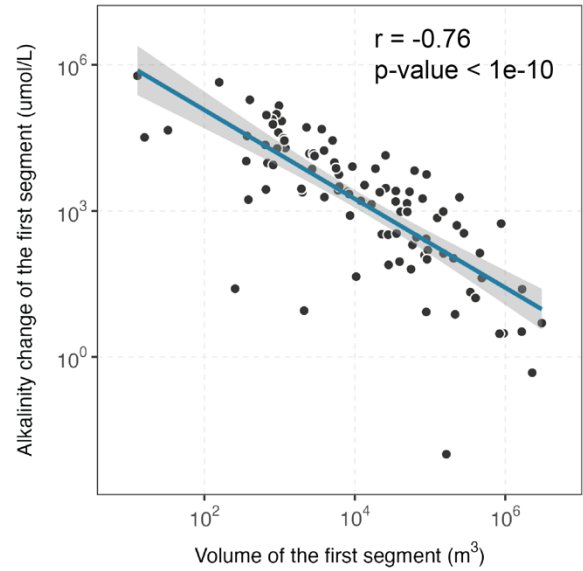


155
 156 **Figure S18.** Alkalinity and the alkalinity/volume ratio through time of each flow path for each
 157 ERW application site. (A) Median alkalinity of river segments for each flow path through time for
 158 each ERW application site. (B) The ratio of alkalinity input flux from the basalt dissolution to the
 159 total volume of river segments for each flow path through time for each ERW application site. The
 160 two symbols in panel A and B represent the two flow paths with the highest leakage rates (see Fig.
 161 2B). Dashed lines in panel A and B represent 6 months, 12 months, 18 months, and 24 months
 162 from left to right.
 163

A

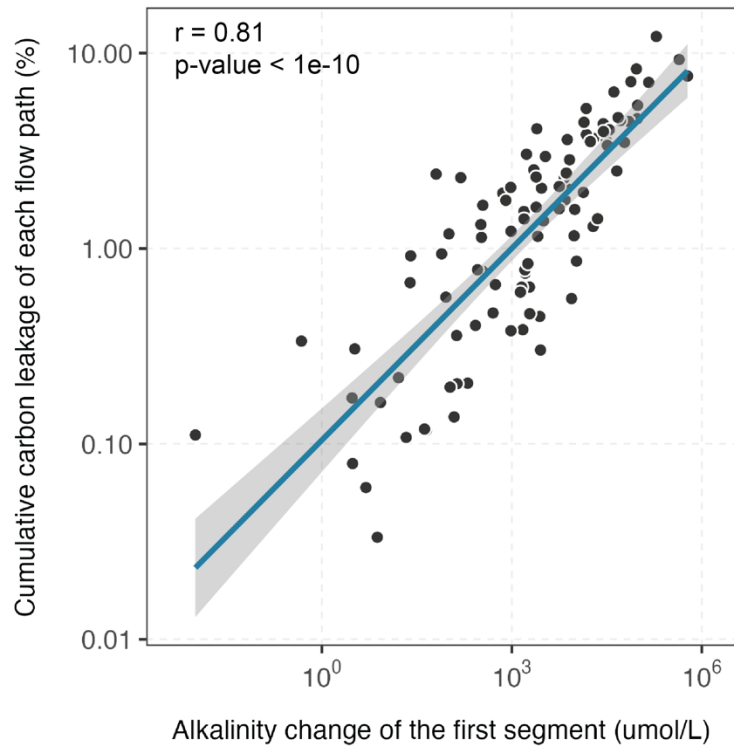


B



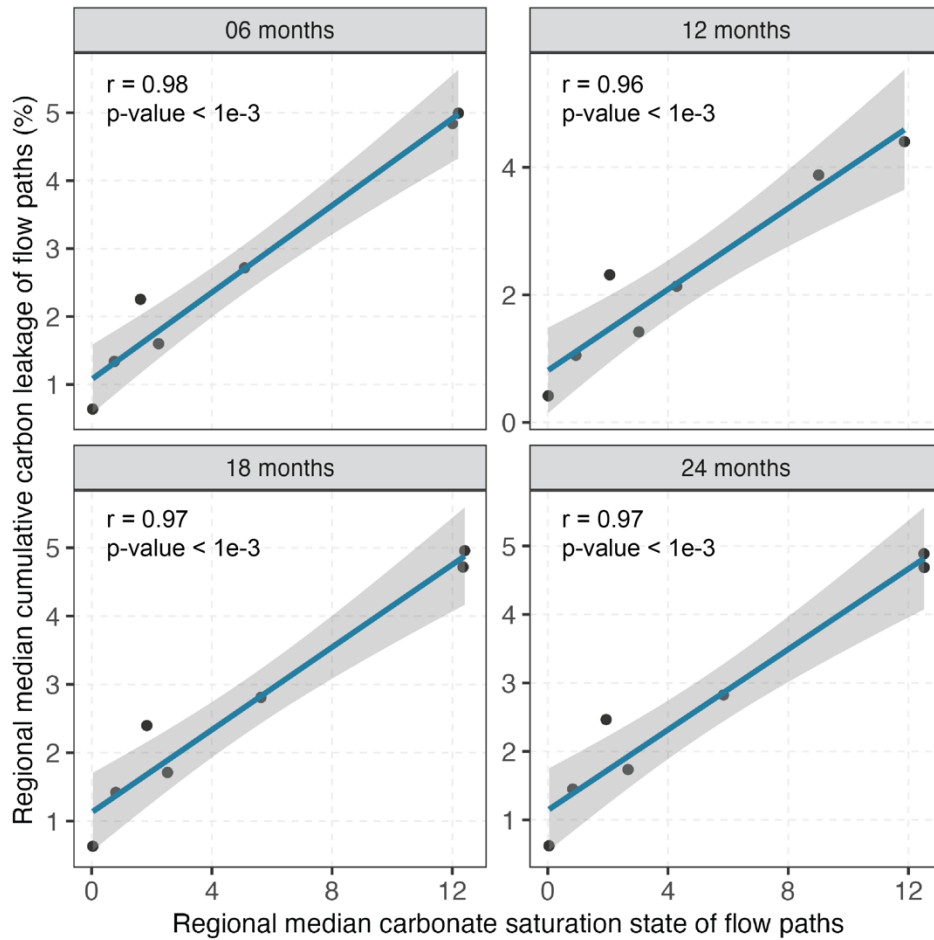
164
165
166
167
168
169
170
171
172
173
174

Figure S19. (A) Correlation between the alkalinity change of the first river segment (relative to its concurrent background state) and the added alkalinity flux for each flow path over duration of 1 day. (B) Correlation between the alkalinity change of the first river segment (relative to its concurrent background state) and the volume of the first segment over duration of 1 day. The correlation coefficient (r) and the p-value are also shown.



175
176
177
178
179

Figure S20. Correlation between the cumulative carbon leakage and the alkalinity change of the first river segment (relative to its concurrent background state) of each flow path over duration of 1 day. The correlation coefficient (r) and the p -value are also shown.



181
 182
 183
 184
 185

Figure S21. Correlation between the regional median carbonate saturation state and the regional median cumulative carbon leakage rate over durations of 6, 12, 18, and 24 months. The correlation coefficient (r) and the p-value are also shown.